arXiv:1907.07193v1 [astro-ph.HE] 16 Jul 2019

A DECAM SEARCH FOR EXPLOSIVE OPTICAL TRANSIENTS ASSOCIATED WITH ICECUBE NEUTRINOS

R. Morgan,[1,2] K. Bechtol,[3,1] R. Kessler,[4,5] M. Sako,[6] K. Herner,[7] Z. Doctor,[5] D. Scolnic,[5] I. Sevilla-Noarbe,[8]
A. Franckowiak,[9] K. N. Neilson,[10] M. Kowalski,[11,12] A. Palmese,[7] E. Swann,[13] B. P. Thomas,[13] A. K. Vivas,[14]
A. Drlica-Wagner,[7,5] A. Garcia,[15] D. Brout,[6] F. Paz-Chinchón,[16] E. Neilsen,[7] H. T. Diehl,[7] M. Soares-Santos,[15]
T. M. C. Abbott,[14] S. Avila,[17] E. Bertin,[18,19] D. Brooks,[20] E. Buckley-Geer,[7] A. Carnero Rosell,[8,21]
M. Carrasco Kind,[22,16] J. Carretero,[23] R. Cawthon,[24] M. Costanzi,[25] J. De Vicente,[8] S. Desai,[26] P. Doel,[20]
B. Flaugher,[7] P. Fosalba,[27,28] J. Frieman,[7,5] J. García-Bellido,[17] E. Gaztanaga,[27,28] D. W. Gerdes,[29,30]
D. Gruen,[31,32,33] R. A. Gruendl,[22,16] J. Gschwend,[21,34] G. Gutierrez,[7] D. L. Hollowood,[35] K. Honscheid,[36,37]
D. J. James,[38] N. Kuropatkin,[7] M. Lima,[39,21] M. A. G. Maia,[21,34] J. L. Marshall,[40] F. Menanteau,[22,16]
C. J. Miller,[29,30] R. Miquel,[41,23] A. A. Plazas,[42] E. Sanchez,[8] V. Scarpine,[7] M. Schubnell,[30] S. Serrano,[27,28]
M. Smith,[43] F. Sobreira,[44,21] E. Suchyta,[45] M. E. C. Swanson,[16] G. Tarle,[30] V. Vikram,[46] A. R. Walker,[14] and
J. Weller[47,48,25]

[1] *Physics Department, University of Wisconsin-Madison, 1150 University Avenue Madison, WI 53706, USA*
[2] *Large Synoptic Survey Telescope Corporation Data Science Fellowship Program*
[3] *Large Synoptic Survey Telescope, 933 North Cherry Avenue, Tucson, AZ 85721, USA*
[4] *Department of Astronomy and Astrophysics, University of Chicago, Chicago, IL 60637, USA*
[5] *Kavli Institute for Cosmological Physics, University of Chicago, Chicago, IL 60637, USA*
[6] *Department of Physics and Astronomy, University of Pennsylvania, Philadelphia, PA 19104, USA*
[7] *Fermi National Accelerator Laboratory, P. O. Box 500, Batavia, IL 60510, USA*
[8] *Centro de Investigaciones Energéticas, Medioambientales y Tecnológicas (CIEMAT), Madrid, Spain*
[9] *Deutsches Elektronen Synchrotron DESY, D-15738 Zeuthen, Germany*
[10] *Department of Physics, Drexel University, 3141 Chestnut St, Philadelphia, PA 19104*
[11] *Institute of Physics, Humboldt-Universität zu Berlin, Newtonstr. 15, 12489 Berlin, Germany*
[12] *Deutsches Elektronen-Synchrotron, D-15735 Zeuthen, Germany*
[13] *Institute of Cosmology and Gravitation, University of Portsmouth, Portsmouth, PO1 3FX, UK*
[14] *Cerro Tololo Inter-American Observatory, National Optical Astronomy Observatory, Casilla 603, La Serena, Chile*
[15] *Brandeis University, Physics Department, 415 South Street, Waltham MA 02453*
[16] *National Center for Supercomputing Applications, 1205 West Clark St., Urbana, IL 61801, USA*
[17] *Instituto de Fisica Teorica UAM/CSIC, Universidad Autonoma de Madrid, 28049 Madrid, Spain*
[18] *CNRS, UMR 7095, Institut d'Astrophysique de Paris, F-75014, Paris, France*
[19] *Sorbonne Universités, UPMC Univ Paris 06, UMR 7095, Institut d'Astrophysique de Paris, F-75014, Paris, France*
[20] *Department of Physics & Astronomy, University College London, Gower Street, London, WC1E 6BT, UK*
[21] *Laboratório Interinstitucional de e-Astronomia - LIneA, Rua Gal. José Cristino 77, Rio de Janeiro, RJ - 20921-400, Brazil*
[22] *Department of Astronomy, University of Illinois at Urbana-Champaign, 1002 W. Green Street, Urbana, IL 61801, USA*
[23] *Institut de Física d'Altes Energies (IFAE), The Barcelona Institute of
Science and Technology, Campus UAB, 08193 Bellaterra (Barcelona) Spain*
[24] *Physics Department, 2320 Chamberlin Hall, University of Wisconsin-Madison, 1150 University Avenue Madison, WI 53706-1390*
[25] *Universitäts-Sternwarte, Fakultät für Physik, Ludwig-Maximilians Universität München, Scheinerstr. 1, 81679 München, Germany*
[26] *Department of Physics, IIT Hyderabad, Kandi, Telangana 502285, India*
[27] *Institut d'Estudis Espacials de Catalunya (IEEC), 08034 Barcelona, Spain*
[28] *Institute of Space Sciences (ICE, CSIC), Campus UAB, Carrer de Can Magrans, s/n, 08193 Barcelona, Spain*
[29] *Department of Astronomy, University of Michigan, Ann Arbor, MI 48109, USA*
[30] *Department of Physics, University of Michigan, Ann Arbor, MI 48109, USA*
[31] *Department of Physics, Stanford University, 382 Via Pueblo Mall, Stanford, CA 94305, USA*
[32] *Kavli Institute for Particle Astrophysics & Cosmology, P. O. Box 2450, Stanford University, Stanford, CA 94305, USA*
[33] *SLAC National Accelerator Laboratory, Menlo Park, CA 94025, USA*
[34] *Observatório Nacional, Rua Gal. José Cristino 77, Rio de Janeiro, RJ - 20921-400, Brazil*
[35] *Santa Cruz Institute for Particle Physics, Santa Cruz, CA 95064, USA*
[36] *Center for Cosmology and Astro-Particle Physics, The Ohio State University, Columbus, OH 43210, USA*
[37] *Department of Physics, The Ohio State University, Columbus, OH 43210, USA*
[38] *Center for Astrophysics | Harvard & Smithsonian, 60 Garden Street, Cambridge, MA 02138, USA*
[39] *Departamento de Física Matemática, Instituto de Física, Universidade de São Paulo, CP 66318, São Paulo, SP, 05314-970, Brazil*
[40] *George P. and Cynthia Woods Mitchell Institute for Fundamental Physics and Astronomy, and
Department of Physics and Astronomy, Texas A&M University, College Station, TX 77843, USA*
[41] *Institució Catalana de Recerca i Estudis Avançats, E-08010 Barcelona, Spain*
[42] *Department of Astrophysical Sciences, Princeton University, Peyton Hall, Princeton, NJ 08544, USA*
[43] *School of Physics and Astronomy, University of Southampton, Southampton, SO17 1BJ, UK*
[44] *Instituto de Física Gleb Wataghin, Universidade Estadual de Campinas, 13083-859, Campinas, SP, Brazil*

Corresponding author: Robert Morgan and Keith Bechtol
robert.morgan@wisc.edu

kbechtol@wisc.edu

[45] *Computer Science and Mathematics Division, Oak Ridge National Laboratory, Oak Ridge, TN 37831*
[46] *Argonne National Laboratory, 9700 South Cass Avenue, Lemont, IL 60439, USA*
[47] *Excellence Cluster Origins, Boltzmannstr. 2, 85748 Garching, Germany*
[48] *Max Planck Institute for Extraterrestrial Physics, Giessenbachstrasse, 85748 Garching, Germany*

ABSTRACT

To facilitate multimessenger studies with TeV and PeV astrophysical neutrinos, the IceCube Collaboration has developed a realtime alert system for the highest confidence and best localized neutrino events. In this work we investigate the likelihood of association between realtime high-energy neutrino alerts and explosive optical transients, with a focus on core-collapse supernovae (CC SNe) as candidate neutrino sources. We report results from triggered optical follow-up observations of two IceCube alerts, IC170922A and IC171106A, with Blanco/DECam (gri to 24th magnitude in ~ 6 epochs). Based on a suite of simulated supernova light curves, we develop and validate selection criteria for CC SNe exploding in coincidence with neutrino alerts. The DECam observations are sensitive to CC SNe at redshifts $z \lesssim 0.3$. At redshifts $z \lesssim 0.1$, our selection criteria reduce background SNe contamination to a level below the predicted signal. For the IC170922A (IC171106A) follow-up observations, we expect that 12.1% (9.5%) of coincident CC SNe at $z \lesssim 0.3$ are recovered, and that on average, 0.23 (0.07) unassociated SNe in the 90% containment regions also pass our selection criteria. We find two total candidate CC SNe that are temporally coincident with the neutrino alerts, but none in the 90% containment regions, which is statistically consistent with expected rates of background CC SNe for these observations. Given the signal efficiencies and background rates derived from this pilot study, we estimate that to determine whether CC SNe are the dominant contribution to the total TeV-PeV energy IceCube neutrino flux at the 3σ confidence level, DECam observations similar to those of this work would be needed for ~ 200 neutrino alerts, though this number falls to ~ 60 neutrino alerts if redshift information is available for all candidates.

Keywords: neutrinos – Supernovae: general – Techniques: photometric

1. INTRODUCTION

The detection of TeV-PeV energy astrophysical neutrinos with the IceCube detector (IceCube Collaboration 2013) has opened a door for multimessenger studies of energetic astrophysical environments (Franckowiak 2017). Such high-energy neutrinos are generally understood to be produced exclusively by the interaction of hardons that have been accelerated to high energies (Abbasi et al. 2011). Neutrinos are largely unaffected by intervening matter and radiation fields and thus can carry information from larger redshifts, and from deeper within opaque sources, than any other particle messenger (Chiarusi & Spurio 2010; Baret & Elewyck 2011). These properties make TeV-PeV energy neutrinos informative probes of high-energy environments, with the potential to provide unique insight to explosive events, such as supernovae (Gaisser & Stanev 1987) and active galaxies (Silberberg & Shapiro 1979), across cosmic time.

In neutrino astronomy, the low neutrino interaction cross section limits the event rate of high-confidence astrophysical neutrinos to a few events per year (Aartsen et al. 2017a). To enable time-domain searches for counterparts to the detected astrophysical neutrinos, the IceCube Collaboration has implemented a realtime alert system for the highest confidence and best localized neutrino events. 22 public realtime neutrino alerts have been issued since 2016 (IceCube Collaboration 2018a), leading to the identification of the first compelling electromagnetic counterpart of a TeV energy neutrino, the flaring gamma-ray blazar TXS 0506+056 (IceCube Collaboration et al. 2018; IceCube Collaboration 2018b). We discuss the connection of TXS 0506+056 to this work in Section 3. The sources of the other 21 alerts remain unknown.

The observed flux for all astrophysical neutrinos with TeV-PeV energies is nearly isotropic, supporting a primarily extragalactic origin (Aartsen et al. 2015a; Ahlers et al. 2016). Several prominent non-thermal and extragalactic source classes, including gamma-ray bursts (Aartsen et al. 2015b), gamma-ray blazars (Aartsen et al. 2017b), and star-forming galaxies (Bechtol et al. 2017), have been suggested and now have stringent upper limits on their total contributions to the IceCube signal. Many analyses have proposed that a subset of core-collapse supernovae (CC SNe) have internal jets and/or shocks that produce prompt TeV-PeV neutrino emission (Thompson et al. 2003; Razzaque et al. 2004; Ando & Beacom 2005; Woosley & Janka 2005; Murase & Ioka 2013, among several others).

In this work, we focus on observationally determining whether CC SNe contribute to the TeV-PeV energy neutrino flux via a prompt neutrino emission mechanism. In order to identify a CC SN associated with a

neutrino alert, follow-up of the event must begin as soon as possible after the neutrino signal–ideally within 1-2 days since some explosion models predict a fast-rising electromagnetic flux on the order of days (González-Gaitán et al. 2015). It is also worth noting that the rise-times of SN explosion models are relatively unconstrained, leading to a challenge in precisely determining the explosion time from observations. Additionally, the high matter densities in collapsing stars are expected to be opaque to gamma-rays (Mészáros & Waxman 2001; Dermer & Atoyan 2003; Senno et al. 2016; Tamborra & Ando 2016), meaning the neutrino signal would lack an accompanying gamma-ray burst. SNe, though, are characteristically bright in the optical bands despite the cosmological distances. Therefore, triggered optical follow-up of the best-localized IceCube neutrino events is an attractive way to search for CC SNe in coincidence with individual neutrino sources (Kowalski & Mohr 2007). We discuss the physical model on which we base our search and its underlying assumptions in Section 2.

For optical follow-up to be feasible, the instrument field of view (FoV) must be matched to the containment region of the neutrino such that there is a high probability of capturing the neutrino source without becoming overwhelmed by false positives. The median angular resolution for neutrinos detected by IceCube with energies above 100 TeV is less than 1 degree (Aartsen et al. 2017c). In addition, the neutrino emission from CC SNe is expected to follow the cosmic star-formation rate, in which case the majority of neutrinos detected at the Earth would be produced by distant sources (Strigari et al. 2005). Therefore, the instrument must also reach an imaging depth sufficient for observing the faint optical signal of the distant CC SNe. This scenario has motivated several optical follow-up efforts, including programs with the Robotic Optical Transient Search Experiment (ROTSE) and the Palomar Transient Factory (PTF) that reach typical limiting magnitudes of 17 and 21, respectively (Aartsen et al. 2015c; Abbasi, R. et al. 2012). The most recent optical follow-up was performed by Pan-STARRS1 (limiting magnitude $\sim$ 22.5, Kankare et al. 2019) in which all transient sources found near five IceCube alerts were found to have no plausible evidence for association with the alerts. One plausible explanation for the lack of neutrino candidates found by these studies is low sensitivity to faint, distant objects. We elaborate on the need for deep imaging in Section 6, and one of the primary goals of this work is to quantify the sensitivity of optical follow-up campaigns to a TeV-PeV neutrino-emitting CC SNe. In this work, we present the deepest optical follow-up to date of IceCube alerts and go beyond the scope of previous studies by characterizing the sensitivity of our follow-up campaign via a maximum likelihood analysis of SNe simulations.

On September 22, 2017 and November 6, 2017, we received alerts for individual $\sim$ 200 TeV neutrinos detected at IceCube with good localization and high probability of astrophysical origin (IC170922A and IC171106A, respectively). We used the Dark Energy Camera (DECam) mounted on the Blanco 4-m telescope in Chile to perform triggered optical follow-up of the two IceCube neutrino alerts. Blanco/DECam's 2.2 deg diameter field of view was able to cover the entire 90% confidence level containment regions in a single pointing for each alert and reached a limiting r-band magnitude of 23.6 mag for a 5σ detection, allowing for a higher sensitivity to CC SNe out to larger redshifts compared to previous efforts. The details of our follow-up observations are presented in Section 3.

As a result of the wide field of view and imaging depth, DECam is capable of finding several hundred transient objects per follow-up. Therefore, to expedite the screening procedure and standardize selection methodology, in Section 4 we present an automated candidate selection pipeline for CC SNe exploding at the time of the neutrino alert. We apply the pipeline to our observations and present the results in Section 5. In Section 6 we supplement our pipeline with calculations of the likelihood of association between a neutrino alert and likely CC SNe selected by the pipeline. We also describe the requirements of an optical follow-up campaign capable of determining whether CC SNe contribute to the TeV-PeV IceCube neutrino flux at a high confidence level. We conclude in Section 7.

2. PHYSICAL MODEL

In this analysis, we evaluate the likelihood that TeV-PeV energy neutrinos detected by IceCube are created by a prompt emission mechanism during the collapse. We take this mechanism to be a relativistic jet within the collapsing massive star (Abbasi, R. et al. 2012) such that hadrons within the star are boosted to TeV-PeV energies. The boost could be caused by several factors, such as shock-breakout or the espresso mechanism (Caprioli 2015). Within the collapsing star, boosted protons could interact with photons, leading to the production of charged pions which would decay to produce energetic neutrinos (Gaisser & Stanev 1987). The high-energy neutrinos then escape the collapsing star due to their low interaction cross section (Beall 2006). We make the assumption that the direction of the internal relativistic jet has no influence on our ability to detect the optical signal of the explosion.

With the above model for the explosion, the multi-messenger signal detectable on Earth would consist of the TeV-PeV energy neutrino, and the electromagnetic signature of a CC SNe. The neutrino signal could be an individual neutrino or a multiplet of neutrinos. A multiplet indicates a closer source, since only in that case is the mean expected neutrino events detected by IceCube expected to be larger than one. The majority of singular neutrino events comes from more distant sources with mean number of expected neutrino events much smaller than one (IceCube et al. 2017; Strotjohann et al. 2019). In this analysis, the alerts we followed-up are single-neutrino alerts. The neutrino signal is expected to be detected on Earth a few hours to ~ 1 day before the electromagnetic signal becomes bright enough to be detectable. This time delay is a direct result of our assumed explosion mechanism: the neutrinos are emitted at the beginning of the explosion and nearly immediately escape the star, while photons are emitted throughout the typically week-scale process and have a much shorter mean-free-path between interactions inside the star. Furthermore, gamma rays created by the prompt neutrino mechanism have a high probability of being absorbed by the dense stellar material, so the majority of the electromagnetic signal would be composed of optical wavelengths delayed by a few hours to ~ 1 day.

To test our hypothesis that CC SNe contribute to the TeV-PeV energy neutrino flux detected by IceCube, we perform a maximum likelihood analysis of the objects found by Blanco/DECam during our triggered follow-up observations. For this analysis, we derive the expected redshift distributions of background SNe and associated CC SNe in Section 4. Our derivation of the signal sample redshift distribution is based on three assumptions: the IceCube Collaboration accurately reports the probability that an observed neutrino is astrophysical (i.e. not created by cosmic rays interacting in the atmosphere), that CC SNe are the sole component of the TeV-PeV energy neutrino flux, and that CC SN redshifts are distributed according to the cosmic massive star formation rate (Madau & Dickinson 2014). We elaborate on our first assumption in Section 3.1. The second assumption is relaxed in Section 6 when we assess the necessities of a sustained optical follow-up campaign for different fractions of CC SNe contribution to the IceCube flux. Lastly, the third assumption is physically motivated since stars with mass greater than $\sim 8 M_\odot$ are expected to end in CC SNe (Burrows et al. 1995).

Based on the final assumption, we obtain the expected redshift distribution of associated CC SNe that we detect in our follow-up observations using the following equation for the cumulative neutrino intensity as a function of redshift:

$$\frac{dN_\nu(E_\nu)}{dE_\nu d\Omega dt_{obs} dA} =$$
$$\int_0^{z_{\max}} \frac{dV}{dzd\Omega} \frac{1}{4\pi D_L^2} \frac{dN_\nu(E_\nu(1+z))}{dE_\nu} \frac{1}{1+z} \mathcal{R}(z)\varepsilon(z)dz. \tag{1}$$

In Equation 1, $dV/(dzd\Omega)$ is the co-moving volume element, $1/(4\pi D_L^2)$ is a division by the surface area of a sphere with radius equal to the luminosity distance, $dN_\nu(E_\nu(1+z))/dE_\nu$ is the predicted number of observed neutrinos with energy E_ν from a CC SN at a given redshift, $1/(1+z)$ is the general relativistic time-dilation factor, $\mathcal{R}(z)$ is the formation rate for stars that will become CC SNe at a given redshift, and $\varepsilon(z)$ is the optical detection efficiency for associated CC SNe. Integrating from $z = 0$ to $z = z_{\max}$ gives the cumulative neutrino intensity from CC SNe which explode up to redshift $z_{\max}$. For this calculation and for the simulations used in Section 4, we adopt a flat ΛCDM cosmology with Hubble constant $H_0 = 67.77$ km s^{-1} Mpc^{-1} following the type Ia SNe measurement made by the Dark Energy Survey (DES Collaboration 2018a). We also take fractions of the universe's energy density made up by matter and dark energy to be $\Omega_m = 0.298$ and $\Omega_\Lambda = 0.702$, respectively, following the combined probe measurements of (DES Collaboration 2018b).

3. OBSERVATIONS AND DATA

In this section we provide background on the instruments used in this analysis and detail the relevant observations. We summarize this section in Table 1.

3.1. *IceCube Real-time Neutrino Alerts*

IceCube is a cubic-kilometer scale neutrino detector located at the geographic South Pole and built into the Antarctic ice at depths ranging from 1450 m to 2450 m (Halzen 2016). Incident neutrinos are detected indirectly through Cherenkov radiation emitted by secondary charged particles produced in the neutrino interaction with nuclei of the ice. Events detected by IceCube are classified as "shower" events or "track" events. Showers are produced in charged-current interactions of electron and tau neutrinos and neutral-current interactions of all neutrino flavors. A shower of secondary particles is produced which has an extension of few meters, which is small compared to the distance between the optical modules. Therefore the Cherenkov light produced by the shower particles appears almost spherical and yields an angular reconstruction of the incoming

IceCube Neutrino Alerts		
Name	IC170922A	IC171106A
Date	22 Sep 2017	6 Nov 2017
Time (UTC)	20:54:30.43	18:39:39.21
Neutrino Energy (TeV)	120.0	230.0
RA (deg)	$77.43^{+0.95}_{-0.65}$	$340.25^{+0.70}_{-0.25}$
Dec (deg)	$+5.72^{+0.70}_{-0.50}$	$+7.31^{+0.35}_{-0.25}$
Containment Region Area (90% C.L.) (deg^2)	0.97	0.57
Signalness	0.56507	0.74593

Blanco/DECam Follow-Ups		
Observing Nights after Alert	1, 3, 10, 20, 21	1, 2, 4, 10, 16
First Night - Alert Time Difference (hours)	10.72	7.22
Filters	$g\ r\ i$[a]	$g\ r\ i\ z$[b]
Exposure Time (s) per Band per Epoch	2×150	2×150
Effective DECam FoV Area (deg^2)	3.12	2.71
5σ Mag Limit (g, r, i)	23.6, 23.7, 23.3	23.4, 23.5, 23.1
Average Airmass	1.24	1.26

Table 1. *Top*: Properties of the two southern-sky, high-energy IceCube alerts observable from CTIO from Aug 2017 through Jan 2018. "Signalness" is described in Section 2.1. *Bottom*: DECam observing cadences and conditions.
[a] Only gr were used on the final observing night.
[b] gri for all nights except the final night, which was riz.

neutrino on the order of ~ 15 deg. Tracks are produced by charged-current interactions of muon neutrinos in or close to the detector, which produce a muon that travels along a long linear path through the ice, providing a good lever arm for the angular reconstruction. Specifically, for track neutrino events with energies above 100 TeV, IceCube achieves median angular resolutions for high-energy starting events (HESE) and extremely high energy events (EHE) of 0.4-1.6 deg and <1.0 deg, respectively. (Aartsen et al. 2014, 2017a).

In an effort to locate the sources of these neutrinos, the IceCube Collaboration has created a real-time alert system for events of likely astrophysical origin in order to facilitate follow-up studies (Aartsen et al. 2017a). The system has a median latency of 33 seconds in which neutrino events are processed and reconstructed, and within three minutes alerts are published to streams such as the Astrophysical Multimessenger Observatory

Network (AMON, Smith et al. 2013; Keivani et al. 2017) and the Gamma-ray Coordination Network (Barthelmy et al. 1998, GCN). Alerts are only published if the event satisfies two-dimensional selection criteria placed on the zenith angle (θ) and the number of photoelectrons (NPE) deposited by the neutrino (Aartsen et al. 2017a). The probability that the neutrino is of astrophysical origin, referred to as the "signalness", is calculated from the expected numbers of signal and background events in the corresponding bin of the two-dimensional parameter space of θ and $\log_{10}$ NPE. For contextual purposes, if the signalness is larger than 0.5, the alert is usually published, but exceptions lie on both sides of this cutoff since the cuts are placed on where the event lies in the θ versus $\log_{10}$ NPE parameter space rather than on the value of the signalness.

On September 22, 2017 IceCube detected a singular high-energy neutrino. Another singular high-energy neutrino was detected on November 6, 2017. Both events had good angular resolution and likely astrophysical origin. The details of the AMON alerts are presented in the top portion of Table 1. Both alerts were track-type singular neutrinos with energies on the 100-200 TeV scale. These alerts featured signalness scores of ~ 0.57 and ~ 0.75 and 90% confidence level containment region areas smaller than the field of view of DECam. The high energies and signalness scores suggest an astrophysical origin of the events and motivate the search for an optical counterpart in form of CC SNe.

Of the 22 alerts issued thus far by the IceCube Collaboration, 12 have occurred after the start of this analysis. Of the 12 possible alerts, nine were either deemed unobservable based on atmospheric, moon, or sun conditions, or were retracted by the IceCube Collaboration. The two alerts presented here are two of only three alerts that have been observable from the location of the Blanco Telescope in Chile. The final alert, IC181023A, was observed and will be discussed in a future work.

### 3.2. *DECam Imaging Follow-up*

The Dark Energy Camera (Flaugher et al. 2015) is a 570-Megapixel optical imager mounted on the 4-m Blanco Telescope at Cerro Tololo Inter-American Observatory (CTIO) in Chile. Blanco/DECam's location, field of view (~ 3 deg^2), and deep imaging capabilities make it the only southern hemisphere imager with a wide field of view matched to the IceCube angular resolution and a large enough aperture to efficiently detect explosive optical transients at the redshifts relevant for proposed neutrino sources.

The Dark Energy Survey (DES) is a wide-field optical survey (expected to reach a 10σ depth for point sources
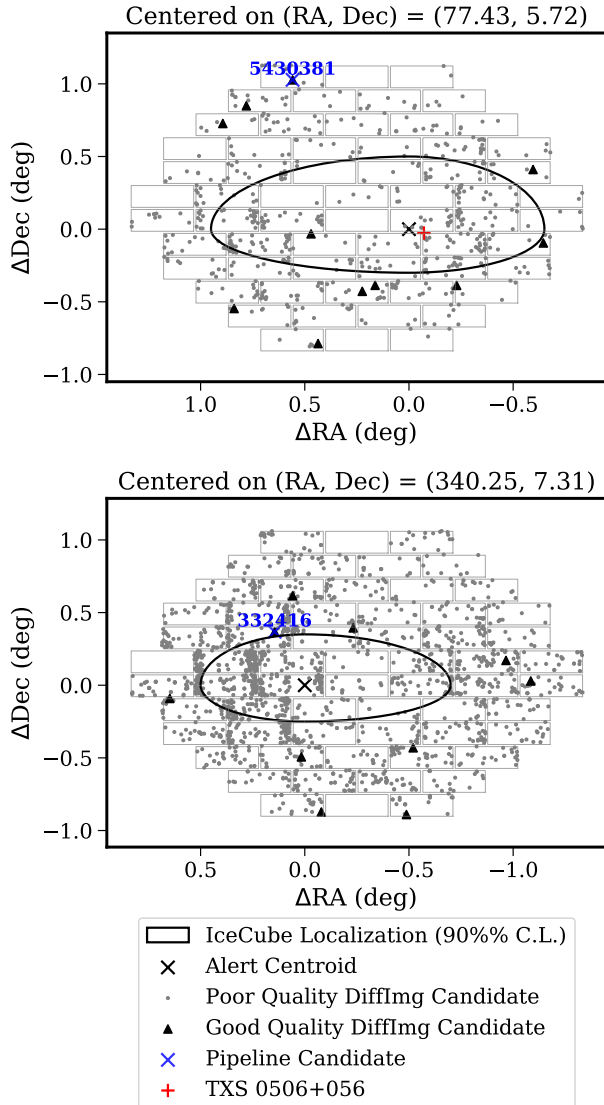
Figure 1. The DECam fields of view for the IC170922A follow-up (*top*) and for the IC171106A follow-up (*bottom*) showing difference imaging products, the containment region for the neutrino at the 90% confidence level, and the candidates selected by our Neutrino Candidate Identification Pipeline (`NCIP`). The location of TXS 0506+056 is also shown for reference.

of $grizY = 25.2, 24.8, 24.0, 23.4, 21.7$ mag over 5,000 deg^2) with 577 full DECam observing nights (Mohr et al. 2012). Operating within a large survey program is ideal for our follow-up study because there is no need to interrupt community observers, and the interruptions are short (20 min). Specifically, we use triggered target-of-opportunity (ToO) observations to promptly respond to IceCube alerts for ~ 20 minutes (co-located 2×150 sec exposures in the gri-bands) per night on ~ 6 nights
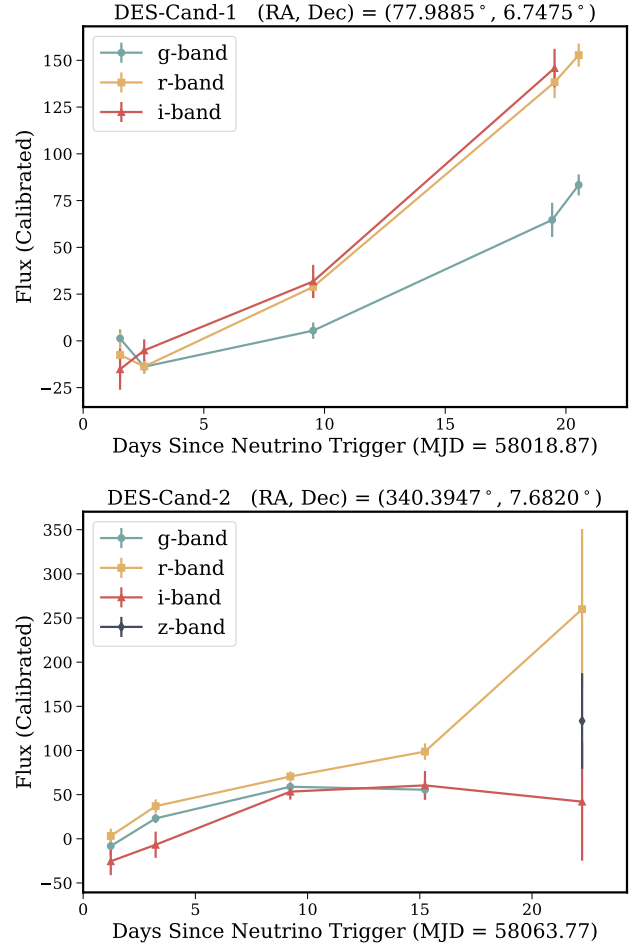
Figure 2. *Top*: Light curves in gri for DES-Cand-1, one of the difference imaging products selected by `NCIP` in the IC170922A follow-up. *Bottom*: Light curves in $griz$ for DES-Cand-2, the candidate from the IC171106A follow-up.

over approximately a three week period after the alert, depending on atmospheric and moon conditions. For the IC170922A follow-up, we dithered by a half chip in RA and Dec between exposures of the same band to fill in chip gaps, leading to a slightly larger effective DECam FoV area in Table 1.

The observing epochs were distributed with two nights immediately after the alert to look for rapidly-fading optical transients and with the remaining nights spread in 5-7 night intervals to observe the rise and peak of potentially-associated CC SNe. Cloudy nights or nights where the moon is bright were avoided, which leads to different cadences for each follow-up. For the IC170922A follow-up, we dithered by a half-chip in each direction to fill in DECam chip gaps, however for the IC171106A follow-up, the same pointing was used for all exposures. Exposures in the same band on the same night were co-added to increase depth.

The DECam observations were processed by the DES Difference Imaging Pipeline (Kessler et al. 2015, `DiffImg`), which subtracts template images from the observations and produces catalog-level photometric fluxes in each band for all detected transients in the field of view. For this analysis, since our observations did not overlap with the DES footprint where template images would be readily available, we use the first night images as templates. Observations are also run through `autoscan` (Goldstein et al. 2015), which identifies potential image artifacts and poor image subtractions. This information is carried to the catalog-level photometric data through the Machine-Learning (ML) score, which can be interpreted as a measure of the probability a `DiffImg` candidate is a real astrophysical object. This score is utilized in Section 4. From the `DiffImg` outputs, objects that are likely CC SNe and temporally coincident with the neutrino alert based on light curve properties are selected by an automated neutrino source candidate identification pipeline described in Section 4. The `DiffImg` products and pipeline candidates for both IC170922A and IC171106A are shown in Figure 1. The light curves of the pipeline candidates are shown in Figure 2.

The Special Case of TXS0506+056

It should be noted here that one of the two alerts discussed in this work, IC170922A, has compelling evidence for association with the flaring gamma-ray blazar TXS 0506+056. We include the location of TXS 0506+056 in Figure 1 for reference. Our choice to follow-up IC170922A with DECam/Blanco was made before the potential association with TXS 0506+056 was determined, hence, we proceed with the analysis as if TXS 0506+056 had not been reported.

This first claim of a neutrino-based multimessenger signal is based on a comparison of 10 years of Fermi-LAT data to observations of TXS 0506+056 in its flaring state by several collaborations (IceCube Collaboration et al. 2018). The coincidence triggered a search for archival neutrinos from the position of TXS which revealed a 158-day long excess of lower energy neutrinos in 2014 and 2015 with a significance of 3.5 σ (IceCube Collaboration 2018b). Cross-correlation studies, though, using a larger neutrino event sample, have found upper limits on the gamma-ray blazar contribution to the diffuse neutrino flux to be $\sim 30\%$ and 1-10% (Aartsen et al. 2017b; Murase et al. 2018, respectively), suggesting that the search for other source classes is still well-motivated.

In the optical bands, TXS 0506+056 was very bright, reaching ~ 14 mag in the V-band for example (IceCube Collaboration et al. 2018). Because our DECam limiting magnitude was ~ 23 mag to search for faint sources, our images pixels were saturated at the particular location of TXS 0506+056. Optical imaging, spectroscopy, and polarimetry for the event were obtained from combination of ASAS-SN, Kanata/HONIR, Kiso/KWFC, Liverpool Telescope, and Subaru/FOCAS (IceCube Collaboration et al. 2018).

4. SENSITIVITY ANALYSIS USING SIMULATIONS

As evidenced by Figure 1, `DiffImg` recovers many moving objects, variable objects, and transients within a typical neutrino localization region including asteroids, active galactic nuclei (AGN), and background SNe. The background SNe population is composed of type Ia SNe, CC SNe exploding before the neutrino alert but persisting into the observing window, CC SNe exploding near the time of the neutrino alert, and CC SNe exploding after the alert but becoming bright enough to be optically detectable before the observing window has concluded. The removal of unassociated transients from our observations is critical for isolating potential neutrino source candidates. We therefore develop selection criteria to remove CC SNe exploding before or much later than the neutrino trigger and type-Ia SNe altogether. The selection criteria applied to the `DiffImg` output are collectively named the Neutrino Candidate Identification Pipeline (`NCIP`). The following analysis demonstrates the extent to which these unassociated transients can be removed from DECam observations while maintaining a high detection efficiency for the potentially associated CC SN.

4.1. *Simulations and Candidate Selection*

Selecting CC SNe associated with IceCube neutrino alerts requires extrapolating the explosion time of the SN from its light curve. To model the rise times of SNe, we employ the SuperNova ANAlysis software suite (`SNANA`, Kessler et al. 2009), which enables us to simulate SN light curves based on our observing cadence. Based on `SNANA` simulated SN light curves for our observations, we develop selection criteria to filter out unassociated SNe. Then by applying the selection criteria to the same simulations, we determine the detection efficiency for an associated CC SN and the expected number of unassociated SNe found by `NCIP` for each follow-up.

We simulated SNe light curves for 500 DECam FoVs for each follow-up. The background population of simulated light curves consists of both type Ia and CC SNe that reach peak brightness in a range of MJDs extending from 30 nights before the observing window to 100 nights after the observing window has concluded. For the simulated type Ia SNe we use templates from (Guy et al. 2010) and rates from (Dilday et al. 2008), and for

	IC170922A Follow-up							
Sample	Signal Efficiency All SNe[a]		Signal Efficiency Optically Detectable SNe[a]		Background Events[a] in IC90		Data[b] in FoV	Data[b] in IC90
Cut	$z < 0.3$	$z > 0.3$	$z < 0.3$	$z > 0.3$	$z < 0.3$	$z > 0.3$	−	−
Total	$1.0000_{-0.0001}$	$1.00000_{-0.00001}$	−	−	9.26 ± 0.14	414.2 ± 0.9	617	240
Quality	$0.199^{+0.004}_{-0.004}$	$2.47^{+0.16}_{-0.15} \times 10^{-3}$	$1.0000_{-0.0006}$	$1.000_{-0.005}$	1.48 ± 0.05	3.96 ± 0.09	11	2
Rising	$0.198^{+0.004}_{-0.004}$	$2.47^{+0.15}_{-0.15} \times 10^{-3}$	$0.9984^{+0.0007}_{-0.0011}$	$1.000_{-0.005}$	1.00 ± 0.04	3.07 ± 0.08	10	2
Phase	$0.179^{+0.004}_{-0.004}$	$2.47^{+0.15}_{-0.15} \times 10^{-3}$	$0.9964^{+0.0012}_{-0.0015}$	$1.000_{-0.005}$	0.51 ± 0.03	1.25 ± 0.05	2	0
Classify	$0.121^{+0.003}_{-0.003}$	$1.26^{+0.11}_{-0.11} \times 10^{-3}$	$0.608^{+0.011}_{-0.011}$	$0.51^{+0.03}_{-0.03}$	0.116 ± 0.015	0.113 ± 0.015	1	0

	IC171106A Follow-up							
Sample	Signal Efficiency All SNe[a]		Signal Efficiency Optically Detectable SNe[a]		Background Events[a] in IC90		Data[b] in Fov	Data[b] in IC90
Cut	$z < 0.3$	$z > 0.3$	$z < 0.3$	$z > 0.3$	$z < 0.3$	$z > 0.3$	−	−
Total	$1.0000_{-0.0001}$	$1.00000_{-0.00001}$	−	−	5.13 ± 0.10	236.4 ± 0.7	1868	646
Quality	$0.134^{+0.003}_{-0.003}$	$7.1^{+0.9}_{-0.8} \times 10^{-4}$	$1.0000_{-0.0008}$	$1.000_{-0.016}$	0.65 ± 0.04	1.46 ± 0.05	10	0
Rising	$0.134^{+0.003}_{-0.003}$	$7.1^{+0.9}_{-0.8} \times 10^{-4}$	$0.9978^{+0.0010}_{-0.0016}$	$1.000_{-0.016}$	0.43 ± 0.03	1.11 ± 0.05	8	0
Phase	$0.130^{+0.003}_{-0.003}$	$7.1^{+0.9}_{-0.8} \times 10^{-4}$	$0.970^{+0.004}_{-0.005}$	$0.986^{+0.010}_{-0.02}$	0.187 ± 0.019	0.39 ± 0.03	2	0
Classify	$0.095^{+0.003}_{-0.003}$	$3.3^{+0.4}_{-0.4} \times 10^{-4}$	$0.713^{+0.012}_{-0.012}$	$0.46^{+0.06}_{-0.06}$	0.047 ± 0.010	0.020 ± 0.006	1	0

Table 2. Application of the candidate selection pipeline to simulations and data for IC170922A and IC171106A. The term "optically detectable" is equivalent to the light curve passing the quality cut. Background event values have a statistical uncertainty of $\pm\sqrt{N/500}$ on the mean number of events generated, corresponding to the number of DECam FoVs simulated. The uncertainties reported for the signal efficiencies give a 68% confidence interval. The numbers of background events reported are scaled to reflect just the events within the IceCube 90% CL containment region. The data in the total row is not expected to match the simulations because it can contain non-SNe transients or bad image subtractions that are removed by the quality cut.
[a] Results presented are based on `SNANA` simulations.
[b] Results presented are the number of remaining candidates from DECam observations.

the simulated CC SNe we use templates from (Kessler et al. 2010) and rates from (Bernstein et al. 2012). We do not include asteroids or AGN in the background sample since those models are not available within `SNANA`, though it has been shown that they can be effectively removed with additional selection criteria (Bailey et al. 2007). The simulated signal population consists of only CC SNe with an explosion time set to be the date of the IceCube neutrino alert. Since explosion times are not observed, CC SNe models are more tightly constrained near peak brightness than during the rising phases, and we therefore use the flux relative to its peak value as a proxy for when the explosion began. Within SNANA, we define the explosion time to be the earliest MJD for which the flux in any band reaches 1% of the peak flux in the rest-frame of the SN. To construct the signal sample, CC SN light curves are scanned for the MJD exhibiting a rise in flux above the 1% peak flux level, and then shifted in time so that the MJD aligns with the desired explosion time. By setting the neutrino trigger to the date of the start of the explosion, we are only considering

prompt neutrino emission in this analysis, rather than neutrino emission that may occur during later stages of the collapse. Both sets of simulations account for the measured point spread function, zero point, and sky noise in each exposure to yield light curve quality representative of the actual DECam follow-up observations. The simulations do not account for uncertainty in the CC SNe luminosity function, which is currently approximated using a Gaussian distribution with a mean and standard deviation determined from observed SNe luminosity (Li et al. 2011).

The process of background removal consists of a series of selection criteria applied to the simulated light curves. We list the criteria here and discuss the motivation for each cut in the remainder of this section.

1. *Quality Cut.* Light curves must have detections on two separate nights, irrespective of the band of the detection. If a light curve passes this cut, we refer to it as "optically detectable".
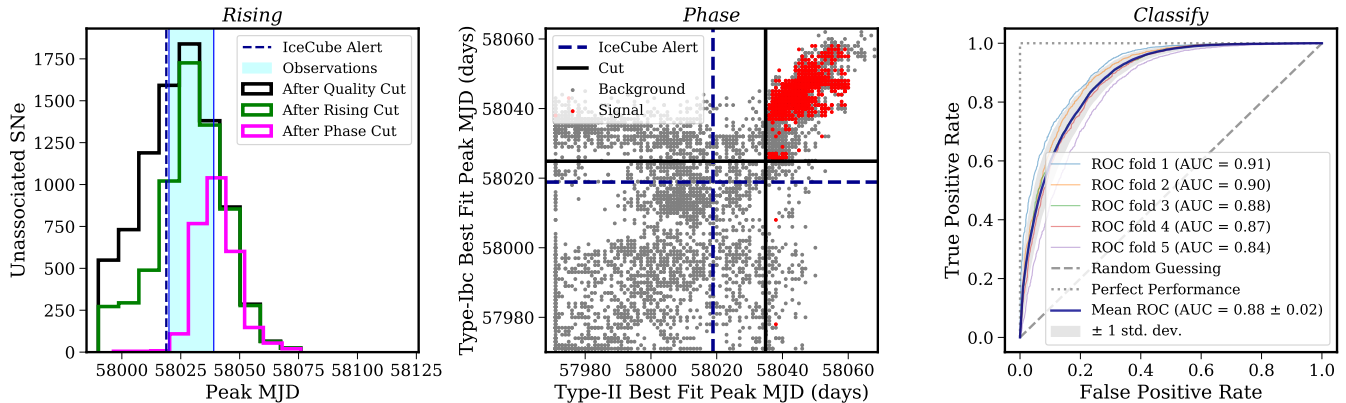
Figure 3. Selection criteria motivation and effectiveness based on simulations of the IC170922A follow-up. *Left*: Distribution of peak MJD values from the background sample after successive cuts. *Center*: Best fit peak MJD values from type II and type Ibc template fits with cuts displayed. *Right*: Receiver Operating Characteristic (ROC) curves of our Random Forest Classifier implemented on 5 folds of the training sample.

2. *Rising Cut.* Light curves must not have a detection on the first post-template night following the trigger, or if there is a detection, there must be an increase in flux of at least one magnitude in at least one band over the first two post-template nights.

3. *Phase Cut.* The peak MJDs predicted by the type Ibc and type II templates fit to the light curve must be at least 6 nights and 16 nights after the trigger, respectively.

4. *Classify Cut.* Light curves must be classified as a CC SN by our Random Forest Classifier.

Quality. The quality cut is designed to guarantee DECam detectability from photometric data quality. For this cut and the rising cut, we define a "detection" in a given band and epoch to mean the photometric data has the following three properties: (1) `DiffImg` finds the object and does not mark it as a bad subtraction; (2) The ML score is larger than 0.7, meaning observation was determined to have good image quality and is unlikely to be an artifact; and (3) the signal-to-noise ratio is larger than 10. The quality cut removes events that are photometrically of too poor quality to claim association with the neutrino by assuring that the event is observable with DECam. In the DECam FoV, we expect 17.5 ± 0.3 SNe and observe 11 objects for IC170922A, and for IC171106A we expect 10.0 ± 0.3 SNe and observe 10 objects. The under-fluctuation for IC170922A is mediated by the application of further cuts.

Rising. The rising cut is designed to select light curves of recently-exploded objects by removing SNe that reach peak brightness before the neutrino trigger. The effectiveness of the rising cut is shown in the left panel of Figure 3. For the two follow-ups presented

here, the first observing night was used to make template images. Therefore, "post-template" nights refer to all nights after the first night. In future follow-ups if it is not possible to observe the field right away, or if template images already exist, this criterion will need to be reformulated. After the rising cut, we expect 13.1 ± 0.3 SNe in the DECam FoV for IC170922A and observe 10 objects, and for IC171106A we expect 7.3 ± 0.3 SNe and observe 8 objects.

Phase. The most differentiating features between the signal and background populations that pass the first level of cuts are the type of SN and where in time the SN exploded relative to the neutrino trigger, which we refer to as the *phase* of the light curve. To exploit these features, we fit all light curves using the `SNANA` implementation of the Photometric SuperNova IDentification tool (Sako et al. 2011, `PSNID`), which offers not only best-fit phase information, but also fit probabilities and χ^2 values for the type Ia, type Ibc, and type II templates fit to each light curve (henceforth χ^2_{Ia}, χ^2_{Ibc}, and χ^2_{II}). The phase cut is designed to remove light curves that exploded before the trigger and are still rising during the observing window. The cutoffs of 6 and 16 nights were empirically derived from analyzing simulations. The motivation for these values is displayed in the center panel of Figure 3, and the performance of the phase cut is also shown in the left panel of the same figure. After the phase cut, we expect 5.6 ± 0.2 SNe in the DECam FoV for IC170922A and observe 2 objects, and for IC171106A we expect 2.74 ± 0.17 SNe and observe 2 objects.

Classify. Since `PSNID` was designed to make classifications with the goal of maximizing type Ia SNe purity, we opted to define two nonlinear features representative of the probability of a light curve being CC in nature in
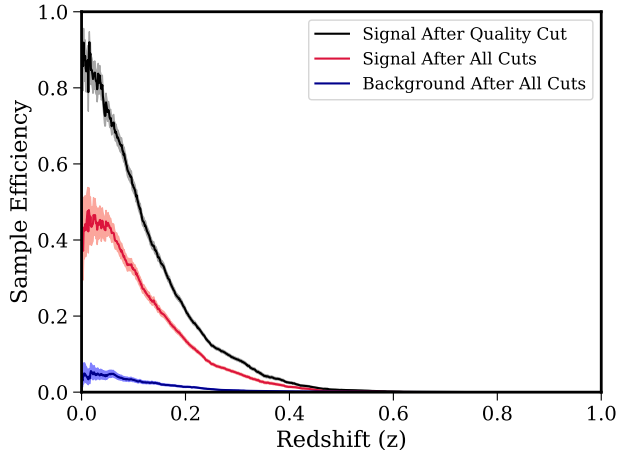
Figure 4. Detection efficiency parameterized by redshift for the signal and background populations based on simulations of the IC170922A follow-up observations. The solid black line illustrates the fraction of CC SNe which would be detectable by DECam, while the solid red line shows the fraction of all CC SNe that pass our selection criteria. The shaded error regions give a 68% confidence interval.

order to maximize CC completeness and minimize the Ia false positive rate. `PSNID` returns χ^2 values for light curve fits to type-Ia ($\chi^2_{\rm Ia}$), type-Ibc ($\chi^2_{\rm Ibc}$), and type-II ($\chi^2_{\rm II}$) templates, Based on this information, we define the normalized Ia and CC χ^2 values $\bar{\chi}^2_{\rm Ia}$ and $1 - \bar{\chi}^2_{\rm CC}$, where

$$\bar{\chi}^2_{\rm Ia} = \frac{\chi^2_{\rm Ia}}{\chi^2_{\rm Ia} + \chi^2_{\rm Ibc} + \chi^2_{\rm II}} \qquad \text{and} \qquad (2)$$

$$\bar{\chi}^2_{\rm CC} = \frac{\min(\chi^2_{\rm Ibc}, \chi^2_{\rm II})}{\chi^2_{\rm Ia} + \chi^2_{\rm Ibc} + \chi^2_{\rm II}}. \qquad (3)$$

Both of the features range from 0 to 1, and are expected to be closer to 0 for a type Ia SN while closer to 1 for a CC SN. Using these features, we reclassified the sample using a Random Forest Classifier (Breiman 2001) implemented with `Sci-Kit Learn` (Pedregosa et al. 2011). To construct the classifier, we first used Principal Component Analysis (Tipping & Bishop 1999, PCA) with 8 components to project light curve fit information to the space of largest variance, and then employed an ensemble of 1000 decision tree classifiers with a restriction of 50 for the maximum tree depth. The number of principal components, number of decision trees, and depth restriction on the decision trees were determined via an extensive search of the hyperparameter space using a separate validation dataset.

The classifier was trained using a `SNANA`-simulated sample of good quality, CC light curves that had an explosion time set to the neutrino trigger and a low redshift ($z < 0.3$) as the target class. The background class

was good quality, CC and Ia light curves determined to be in phase with the neutrino trigger based on best-fit peak MJD. We also include spectroscopically-confirmed CC SNe and Ia SNe from the DES 3 Year SNe sample (DES Collaboration 2018a) in the training set signal and background samples, respectively. All simulated and real SNe in the background sample have a random peak MJD, and hence random explosion time, with the constraint that the light curves satisfy the phase cut. The ratio of simulated SNe to real SNe in the training set was found to strongly correlate to classifier accuracy, and we determined the optimum ratio for each follow-up using an independent validation set. In Figure B.3 we show that optimum classification accuracy on a mixed sample of real SNe and simulated SNe is reached when 36% of the training set is simulated SNe for IC170922A and when 40% of the training set is simulated for IC171106A. The dependence in classification accuracy on the inclusion of real SNe is likely due to the fact that the real SNe were observed under better conditions than our follow-ups. Since our classifier uses best-fit properties to make predictions, it is sensitive to how well the light curve fitting reflects the true properties of the explosion, so the better observing conditions of the real SNe could add new classification information that a simulated training set lacked.

In the process of training, we used stratified 5-fold cross validation to limit overfitting. The classifier operates at 83.7% purity, 68.1% completeness and with a 7.3% false positive rate on the training set and at 81.8% purity, 66.7% completeness, and with a 8.1% false positive rate on the testing set. The similarity of the performance of the classifier on familiar and unseen data is a good indicator that the classification is not suffering from overfitting and will be able to generalize to other datasets. A Receiver Operating Characteristic curve for our classifier is displayed in the right panel of Figure 3 and shows the classifier operating with a 0.88 ± 0.02 area under curve (AUC). After this final cut, we expect 0.74 ± 0.07 SNe in the DECam FoV for IC170922A and observe 1 object, and for IC171106A we expect 0.32 ± 0.06 SNe and observe 1 object. These two remaining objects are our candidates from these first two follow-up efforts.

4.2. Sensitivity Results

We applied the selection criteria to our `SNANA` simulations of the signal and background samples. For the signal samples we report the fraction of events passing each successive cut, as well as the fraction of optically-detectable events passing each successive cut. These fractions are multiplied by the CC SN rate to determine
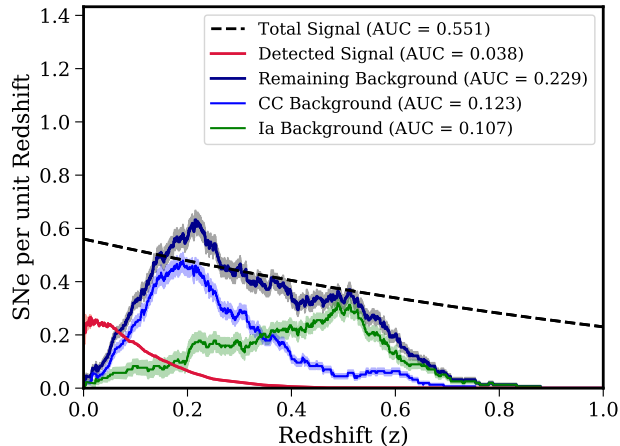
Figure 5. Predicted number of events versus redshift based on simulations of the IC170922A follow-up after the selection criteria have been applied. Shaded error regions give a 68% confidence interval for the signal curve and a standard Poisson statistical uncertainty for the background curves. The AUC shows the cumulative number of expected events in the solid angle of the IceCube 90% containment region.

the expected number of signal-like events per IceCube alert as a function of redshift and scaled to the IceCube 90% confidence level containment region (IC90). The number of background events passing each cut was normalized based on the number of FoVs generated to accurately reflect the expected number of background-like events per follow-up. These results are presented for each of the two events in Table 2.

For events with observing conditions of similar quality to the IC170922A follow-up, we expect to detect roughly 12.1% of nearby ($z < 0.3$), neutrino-emitting CC SNe using DECam and `NCIP`, while limiting the background to 0.23 unassociated SNe up to redshift $z = 1$ within IC90. For the events similar to the IC171106A follow-up observations, we expect to detect 9.5% of nearby signal events and 0.067 background events within IC90 per follow-up. The low signal detection efficiency is a result of the faintness of CC SNe and the magnitude limit of DECam, rather than the strictness of our selection criteria, evidenced by roughly 90% of optically-detectable, low-redshift signal events passing all cuts across both events. The remaining SNe background sample's magnitude, temporal, and redshift distributions are displayed in Figure 6.

Next, we consider the signal detection efficiency and number of remaining background events per set of follow-up observations as functions of redshift in order to calculate the maximum redshift to which we will be able to detect the potential CC SN counterpart of an IceCube alert. These relationships are shown for
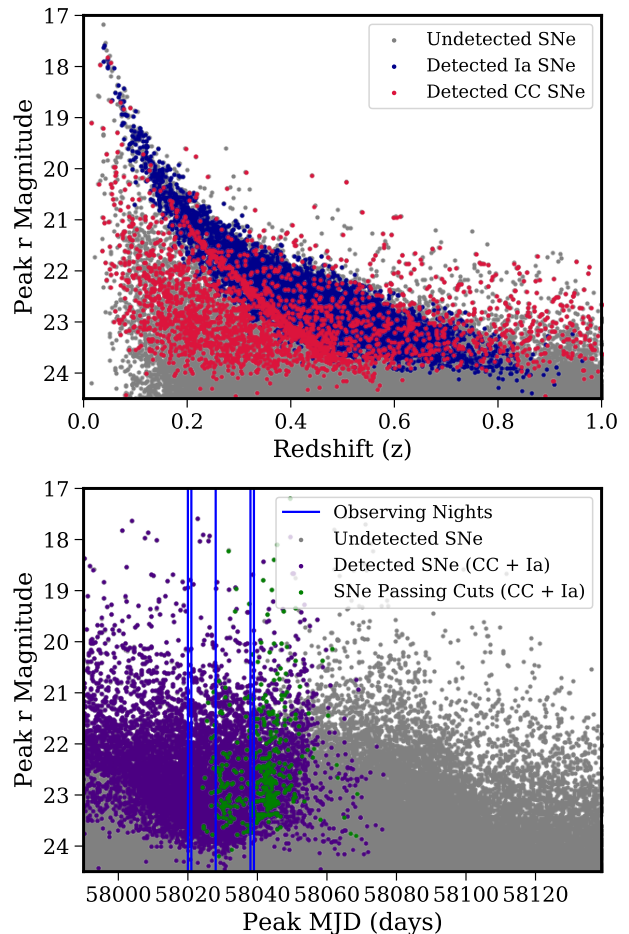
Figure 6. The remaining SNe background events for the IC170922A simulations. *Top*: Peak r-band magnitude versus the MJD of largest flux with reference MJD's of the IceCube alert and the DECam observing nights. *Bottom*: Peak r-band magnitude versus redshift. Both figures display 500 times as many events as would be expected in a single DECam field of view.

the IC170922A follow-up in Figure 4. Based on Figure 4, the fraction of signal sample events remaining after all cuts quickly diminishes as redshift increases, however, this behavior is largely a result of the low optical detectability of high redshift CC SNe.

The distribution of remaining background events per set of follow-up observations based on the observing conditions of the IC170922A follow-up is shown as a function of redshift Figure 5. We note that the type Ia SNe background has been suppressed in the redshift range of highest sensitivity (approximately $z < 0.2$). Therefore, only events that are similar to the signal population in both SN type and phase remain in the final SNe background population. The background sample of this analysis was normalized within `SNANA` such that the

number of events generated was equal to the expected number of SNe within a DECam FoV. The signal sample is normalized to one CC SNe, since only 1 or 0 signal CC SNe is possible per follow-up. The redshift distribution is derived by folding the detection efficiency as a function of redshift with the cosmic star formation rate as described in Section 2. We also multiply the signal distribution by the IceCube signalness value, which is the probability that the neutrino has an astrophysical origin.

From the signal and background redshift distributions, we integrate over all redshifts to obtain the total number of expected signal and background events for a given follow-up. These numbers are displayed on Figure 5 as the Area Under Curve (AUC) values and become important when redshift information for pipeline candidates is unavailable, requiring us to account for all events along the line of sight. Next, we compare the expected number of detected CC SNe associated with the IceCube alert to the number of unassociated SNe expected to pass our selection criteria in a single follow-up observation. Figure 5 displays this comparison for the IC170922A follow-up. The signal clearly dominates the background at low redshifts, and the cumulative number of signal events dominates the cumulative number of background events until roughly $z = 0.3$, which corresponds to the redshift at which associated CC SNe become too faint to detect.

5. RESULTS OF DECAM OBSERVATIONS

We apply our candidate selection pipeline to the difference imaging results for the IC170922A and IC171106A follow-up efforts. We apply two additional selection criteria to our observations for effects that were not simulated. First we exclude candidates that move 0.1 arcseconds or more between observations to exclude asteroids. This cut did not remove anything that was not already removed by the quality cut. Second we perform a catalog search of all pipeline candidates and exclude objects with an angular separation less than 0.4 arcseconds from a known AGN or quasar. This criterion removed 1 candidate from each follow-up. For each DECam follow-up, we display the number of potential candidates remaining after each successive cut in the rightmost column of Table 2. One difference imaging candidate passed all cuts from IC170922A (DES-Cand-1), and one candidate passed all cuts for IC171106A (DES-Cand-2).

For the candidates found by NCIP, the coordinates and IceCube 90% confidence intervals are shown in Figure 1, the light curves are shown in 2, and image stamps are shown in Figures B.1 and B.2. As shown in Table 2, the number of expected SNe to pass our selection criteria per follow-up is between 0 and 1, so it is likely that

IC170922A Follow-Up Candidates

Name	RA (deg)	Dec (deg)	z	Prob.
DES-Cand-1	77.9885	6.7475	–	0.0

Test Statistic:	0.0
p-value:	> 0.999

IC171106A Follow-Up Candidates

Name	RA (deg)	Dec (deg)	z	Prob.
DES-Cand-1	340.3947	7.6820	0.31	0.1055

Test Statistic:	0.0558
p-value:	0.0250

Global Test Statistic:	0.0143
Global p-value:	0.0930

Table 3. NCIP candidates for each follow-up and results of maximum likelihood analysis. The uncertainties on the RA and Dec from DiffImg are negligible and the uncertainty on the redshift of DES-Cand-2 is ±0.02. The rightmost column is the probability that the candidate is associated with the neutrino based on the expected signal and background events in the spatial bin of the candidate. The details of the likelihood analysis are presented in Appendix A. The p-values refer to the hypothesis test of CC SNe contributing the to IceCube neutrino flux as a population, rather than the association between the neutrino and candidate.

these candidates are SNe. The light curves display a clear rise and the image cutouts show a transient object within a host galaxy. A photometric redshift estimate was found for DES-Cand-2 using the methods of (DES Collaboration et al. 2019) which employed a machine learning approach described in (Sadeh et al. 2016). This approach requires exposures in at least four bands, so we were not able to apply it to DES-Cand-1.

For the candidates selected by NCIP, we determined the probability that each candidate was associated with the neutrino source based on the numbers of expected signal and background events in the spatial bins of the candidate. This process is detailed in Appendix A. We also used the candidates to test the hypothesis that CC SNe contribute to the total IceCube neutrino flux. The significance levels of the hypothesis tests and the individual candidate probabilities are displayed in Table 3. The detected candidates are consistent with the expected backgrounds derived in this analysis, hence we do not claim association between our candidates and the neutrino alerts. However, the observed numbers of SNe in the vicinity of IceCube neutrino alerts are in a $\lesssim 1\sigma$ excess of the expected background.

6. FOLLOW-UP STRATEGY IMPLICATIONS

In this section, we examine the viability of optical follow-up campaigns in observationally determining whether CC SNe contribute to the TeV-PeV IceCube neutrino flux given the results and analysis methods presented above. We discuss our results in this context and outline the required components of a successful campaign in the process. We then expand on the analysis by forecasting the requisite number of follow-ups to make a statistically significant statement about this problem.

6.1. *Necessary Observational Components*

Previous efforts have been made to associate CC SNe with neutrino telescope alerts. ROTSE and TAROT were used in optical follow-ups of 42 ANTARES neutrino alerts, reaching a maximum r-band limiting magnitude of 18.6 with a field of view diameter of 2 deg (Adrián-Martínez et al. 2016). One neutrino doublet IceCube alert has been followed up with ROTSE and PTF, and while a CC SN was found in the field of view, it was determined to be old and type IIn via spectroscopy from Keck I LRIS and Gemini/GMOS-N, and therefore unassociated with the neutrinos (Aartsen et al. 2015c). The optical instruments in this effort reached a peak r-band limiting magnitude of 19.5 with a field of view diameter of 2.0 deg. Only a small fraction of cosmic neutrinos will be detected as doublets, while the large majority will be singlets. Accordingly, the follow-up of singlets is a promising approach. However, as shown by Figure 6, significantly deeper observations are required in the singlet case. Specifically, our SNANA simulations, with peak r-band magnitudes displayed in Figure 6, show the importance of DECam's imaging depth in searches for CC SNe since the fainter SNe in the 21-23.5 magnitude range become detectable. A complementary version of Figure 6 where the limiting magnitude was set to 21 mag is available in Figure B.10, illustrating the small fraction of all occurring SNe detectable at this optical depth. Because CC SNe are expected to follow the cosmic massive star formation rate, they are expected to be mostly distributed at higher redshifts, and hence faint in the optical bands. Therefore, it is not surprising that deep imaging offers a significant advantage to follow-up campaigns.

Even with the deep DECam observations presented in this work, detecting a CC SN as a TeV-PeV neutrino counterpart is still difficult as our sensitivity analysis suggests. Our simulations and NCIP analysis show that only $\sim 9.5 - 12$ % of associated CC SNe with $z \leq 0.3$ would be bright enough to be detectable. For $z > 0.3$, less than one percent of associated CC SNe can be detected. When we fold this low detection efficiency with the cosmic massive star formation rate as described in

Section 2, unassociated SNe are expected to overwhelm the signal population. For example, based on the expected signal (0.038) and background (0.229) candidates per follow-up from Figure 5 for IC170922A, we would detect approximately 4 associated CC SNe and 23 unassociated SN out to a redshift of $z = 1.0$ within the IC90 regions over the course of 100 IceCube follow-up experiments using DECam.

The redshift distribution and SN type composition of the expected background after our candidate selection pipeline is displayed in Figure 5, and is particularly useful in understanding the difficulty of claiming association between a neutrino and a CC SNe. In Figure 5, the black curve is the total expected number of signal events for a given follow-up. We have multiplied the redshift probability distribution function described by the cosmic massive star formation rate by the IceCube signalness for the alert, which was ~ 0.56 for IC170922A. This curve also follows the assumption that the entire IceCube TeV-PeV energy neutrino flux is caused by CC SNe, which we refer to as the $\lambda = 1.0$ case in Appendix A. We note that for low redshifts ($z \lesssim 0.2$), the redshifted neutrino energy will be very close to its rest frame energy. Therefore, we find it sufficient to leave out the contribution of the spectral energy distribution of neutrinos from the calculation. The red curve then folds the black curve with the signal detection efficiency from Figure 4 to obtain the expected number of detected CC SNe TeV-PeV neutrino counterparts per follow-up as a function of redshift. In the redshift range where the red curve is non-vanishing, we note that the most dominant background is CC SNe that are present in the FoV but are not associated with the neutrino. These CC SNe have also passed the rising and phase cuts of our pipeline, meaning they appear to be temporally coincident with a neutrino as well. Therefore, the largest background in this analysis is CC SNe that are temporally coincident with the neutrino, which unfortunately are the exact characteristics of our signal population.

Given this background, our main tool for determining if a given candidate is associated with the neutrino alert is the proximity of the candidate to the alert centroid. Additional differentiating features between signal and background samples are the candidate redshift and spectroscopic characterization. The redshift can likely be determined to sufficient accuracy based on a photometric redshift of the host galaxy, but if spectra can be obtained then it would also be possible to exclude the type Ia SNe background.

6.2. *Forecasting Statistical Significance*
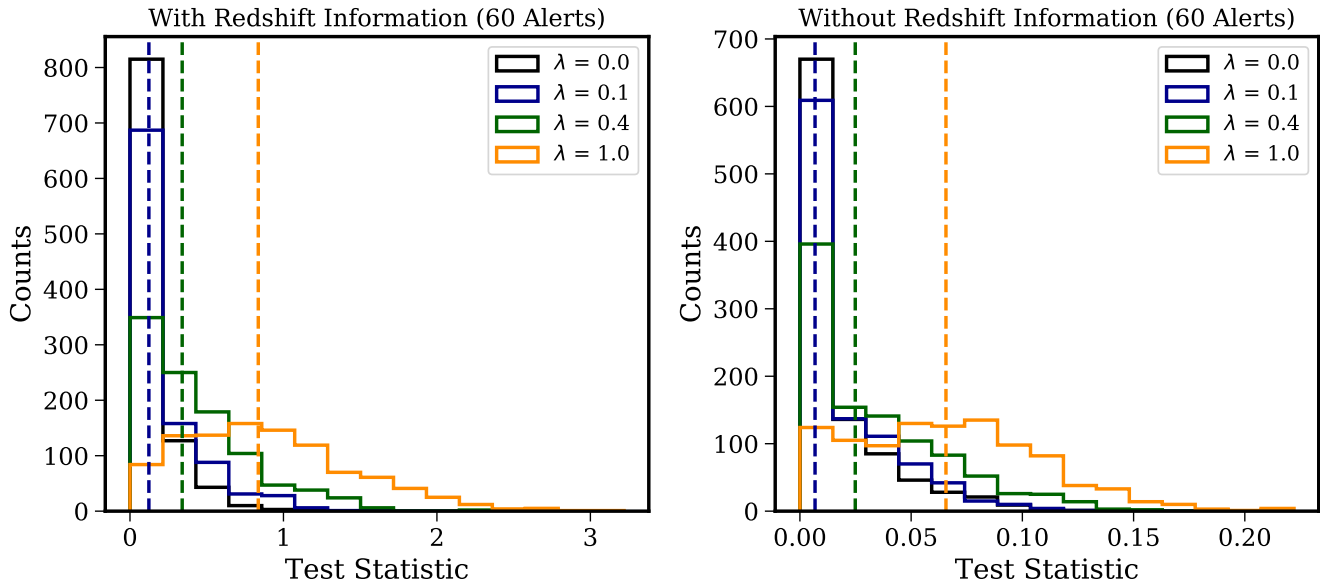
Figure 7. Test statistic distributions for 1000 realizations of the follow-up of 60 IceCube alerts with DECam parameterized by the expected fraction of IceCube events caused by CC SNe (λ). The left/right panel displays the test statistic distribution with/without redshift information available for all alerts. The median values of the signal-hypothesis test statistic distributions are also displayed.

An individual follow-up with deep optical imaging, triggered observations, and redshift information for all candidates is still unlikely to reach a meaningful level of significance due to a signal-like background of unassociated CC SNe that are coincident in time with neutrino alerts and a low signal detection efficiency. Therefore, we frame this analysis as seeking to detect an excess of CC SNe located near IceCube neutrino alerts in space and time over the course of multiple follow-ups. We present a full calculation later in this section, but we outline the basis of it here and restrict our focus to the IC90 region for clarity; the full calculation utilizes the entire DECam Fov. In the IC90 region, from Figure 5 we expect 0.038 signal events and 0.229 background events for a follow-up similar to IC170922A and from Figure B.6 we expect 0.047 signal events and 0.067 background events for a follow-up similar to IC171106A. In the full calculation, if redshift information is available, the contribution to the total significance is weighted by the expected number of signal and background events at the particular redshift. Overall, this process just reduces the contribution of background events to the total significance, so we can account for the effect of having redshift information for a candidate by dividing the expected background by a factor of ~ 3 to simulate a smaller redshift range. Applying this factor and averaging the two follow-ups leads to a mean expected 0.043 signal events and a mean expected 0.049 background events. We then estimate the significance after N follow-ups using a Pois-

son distribution:

$$\text{p-val } = 1 - \text{PoissonCDF(Observed|Expected)}. \quad (4)$$

Setting the "Expected" number of events to be $N \times 0.049$ for the background-only null-hypothesis and setting the "Observed" number of events to be $N \times (0.043 + 0.049)$ enables us to evaluate the significance as a function of the number of follow-ups. As well, one can see that increasing the number of follow-ups will increase the global significance. In this brief calculation, for 100 follow-ups we would expect to reach a p-value of ~ 0.029, which is between 2σ and 3σ. The addition of positional information and a more accurate accounting of redshift information in the full calculation both increase the significance beyond this simplified example.

To make this calculation more rigorous, we simulate pipeline candidate events with frequencies matching the mean expected event rates from the two follow-ups. To determine the probability of a NCIP candidate being the source of the neutrino, we evaluate the candidate's position and redshift in the context of the expected signal and background population distributions of these quantities. For the signal sample, we fit independent 2D asymmetric Gaussian distributions to the 90% confidence level error bounds on the RA and Dec. We multiply our detection efficiency by the fraction of events that would fall on a DECam CCD to account for chip gaps and the few events that fall outside the DECam FoV. For the background distribution, we adopt a uniform distri-

bution of events on the individual DECam CCDs. The redshift distributions for the signal and background samples are taken from Figure 5. Using these distributions, we assess whether CC SNe contribute to the TeV-PeV neutrino flux by searching for an excess of temporally coincident CC SNe in our observations compared to the expected background contamination rate. Appendix A explains this process in greater detail, and overviews the maximum likelihood formalism used to quantify the likelihood of association between our pipeline candidates and IceCube neutrino alerts.

Using the maximum likelihood framework and the angular and redshift distributions for the signal and background samples, we perform 1000 realizations of optical follow-up campaigns of IceCube alerts. For each alert follow-up we determine a list of candidates by sampling the signal and background event distributions. The list of candidates has a probability of containing a signal event of $0.038 \times 0.89 = 0.0338$ for the IC170922A follow-up, where 0.038 is the expected number of detected signal events per follow-up from Figure 5 and 0.89 is the fraction of the signal that falls on the DECam CCDs. We determine the number of background type candidates to simulate using a Poisson probability mass function with mean set to 0.717, which is the number of expected background events per follow-up within the entire DECam FoV calculated from the remaining background AUC in Figure 5 scaled to the area of the full DECam FoV. Once the number of candidates has been determined, we sample the angular and redshift distributions to obtain a realistic representation of the follow-up. We also introduce a signal normalization parameter, λ, which represents the fraction of the TeV-PeV neutrino flux caused by CC SNe, and perform the realizations under different values of λ.

The test statistic distributions for 1000 realizations of follow-up campaigns of 60 alerts based on the conditions of both alerts are displayed in Figure 7. We determine the significance level at which we would be able to claim CC SNe contribute to the TeV-PeV IceCube flux by taking the median value of our alternative hypothesis ($\lambda \neq 0.0$) distributions and calculating the fraction of the null hypothesis distribution ($\lambda = 0.0$) greater than the median test statistic. This fraction can be interpreted as the frequentist p-value. Figure 7 shows that our sensitivity for detecting an excess of CC SNe temporally and spatially coincident with IceCube alerts is greater when redshift information is available and if CC SNe make up a large fraction of the TeV-PeV neutrino flux.

We then further the analysis of the viability of this type of study by calculating the discovery potential for follow-up campaigns with increasing numbers of alerts. The result of this calculation is displayed for the same three values of λ in Figure 8. The cases of every candidate having available redshift information and no candidates having available redshift information are taken as the boundary cases of the best and worst case scenarios. We note that a few alerts are required before the p-value is expected to differ from 1.0 in all cases, but that this behavior is explained by the fact that we use the median test statistic to calculate the p-value. The consequence of this metric is more than 50% of the realizations must have a test statistic above 0.0 for a p-value less than one to be achievable, and it takes a certain number of alerts to reach that point. Based on this calculation, optical follow-up campaigns of this nature would require approximately 60 follow-ups before an excess of temporally and spatially coincident CC SNe could be detected at the 3σ confidence level in the case that photometric redshift information is available for each candidate and that CC SNe account for 100% of the TeV-PeV neutrino flux. In the less optimistic case where CC SNe account for a smaller percentage of the TeV-PeV neutrinos, or redshift information is unable to be obtained, the required number of follow-ups can easily exceed 200. The IceCube event rate is approximately 1 alert per month, and typically 1 in every three alerts is observable from CTIO based on solar and atmospheric conditions.

This analysis highlights several vital components for successful optical follow-ups of IceCube neutrino alerts searching for CC SNe. First, deep imaging is needed to efficiently detect CC SNe counterparts to TeV-PeV neutrino at $z \sim 0.1$, as shown by the comparison between Figures 6 and B.5. A sufficiently large FoV is also required such that the IceCube localization region can be covered. DECam's ~ 23.5 r-band limiting magnitude in 90 second exposures and ~ 3 deg^2 FoV make it the current imager of choice in the southern hemisphere for this task. Even with DECam, we anticipate a large background of CC SNe that are unassociated with the TeV-PeV neutrinos and difficult to distinguish from a neutrino-causing CC SNe. Photometric redshifts and spectroscopic characterization can help with the differentiation, but with the low IceCube event rate and optical detection efficiency of CC SNe, a follow-up campaign would take several years to be able to observe a significant excess of CC SNe near Icecube alerts. It is also possible that tightened constraints on the CC SNe luminosity function and SNe rise times will improve the accuracy of the simulations used in this analysis and in the significance forecasting. It is anticipated that an expansion of the IceCube detector and/or improved realtime alert selection could increase the event rate and
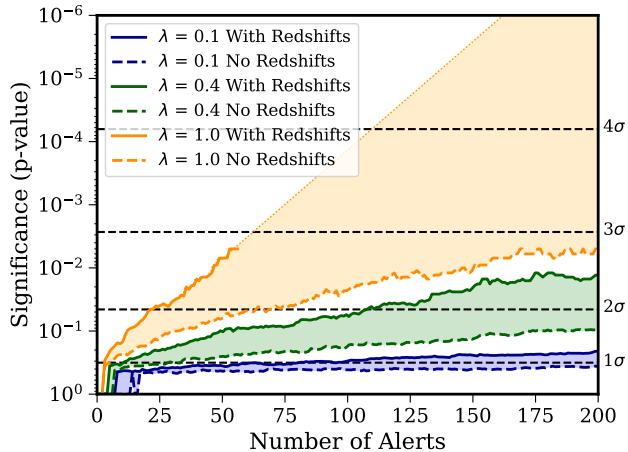
Figure 8. Projected significance levels for DECam follow-up campaigns with increasing numbers of alerts based on the expected numbers of signal and background events in the IC170922A and IC171106A follow-ups. We display the relationship under different values of the parameter λ, which represents the true fraction of the IceCube TeV-PeV neutrino flux caused by CC SNe. We performed 1000 realizations of each follow-up campaign and calculate the p-value by comparing the median test statistic to the null hypothesis test statistic distribution. Since we only performed 1000 realizations, we are unable to probe p-values lower than 0.001, and therefore we extrapolate all p-values smaller than 0.001.

improve the angular resolution of neutrino reconstruction.

7. CONCLUSION

The real-time alert system for IceCube neutrinos has made possible the detection of electromagnetic counterparts for transient high-energy astrophysical events. Using this system, we test whether CC SNe contribute to the largely unexplained TeV-PeV IceCube neutrino flux via a prompt relativistic jet mechanism during the collapse. In this study we followed-up two IceCube alerts from September 22, 2017 (IC170922A) and November 6, 2017 (IC170922A) with photometric observations in optical wavelengths using DECam. These pilot observations combine the deepest-to-date optical follow-up observations of TeV-PeV IceCube neutrinos with a detailed estimation of the relevant backgrounds and a maximum likelihood analysis to fully characterize our sensitivity to CC SNe.

We developed and validated an automated candidate selection pipeline (`NCIP`) based on SNe simulations matched to our observing cadence and conditions. Between the two alerts, `NCIP` found 2 plausible neutrino source candidate SNe (DES-Cand-1 for IC170922A and DES-Cand-2 for IC171106A) based on light curve properties and temporal coincidence. Both candidate SNe

are located outside the respective 90% confidence localization regions from IceCube. Applying a maximum likelihood analysis to our candidates based on the simulated SNe background and spatial coincidence, we find that the two observed candidates are consistent with background unassociated SNe (p-value = 0.093).

To assess the viability of continued optical searches triggered by IceCube alerts, we perform 1000 realizations of follow-up campaigns of up to 200 alerts. We find that approximately 60 follow-ups are required to reach the 3σ confidence level in the case that the astrophysical neutrino flux is contributed entirely by CC SNe and redshifts are available for all detected candidates (Figure 8). Without the availability of photometric redshift information for all candidates, the requisite number of follow-ups rises to ~ 200 to make the same statement. Furthermore, if neutrinos from relativistic jets inside CC SNe do not make up a large percentage of the TeV-PeV neutrino flux, the number of follow-ups required to achieve a high confidence detection could be much larger. The sensitivity is limited primarily by the rate of unassociated low-redshift CC SNe that explode in spatial and temporal coincidence with the neutrino alerts. This residual background is degenerate with the signal population, and therefore challenging to further reduce. Based on the methods presented here and the current rate of HESE and EHE realtime alerts from IceCube, a sustained optical follow-up program using a few hours of DECam time per semester extending over $\gtrsim 10$ years would be needed to determine whether CC SNe contribute to the neutrino flux.

Facility: Blanco (DECam)

Software: PSNID (Sako et al. 2011), SNANA (Kessler et al. 2009), matplotlib (Hunter 2007), pandas (McKinney 2010), numpy (Van Der Walt et al. 2011), sci-kit learn (Pedregosa et al. 2011), scipy (Jones et al. 2001)

APPENDIX

A. MAXIMUM LIKELIHOOD FORMALISM

In this appendix we describe the formalism used to quantify the statistical power of our analysis in terms of testing the hypothesis that CC SNe contribute to the IceCube high-energy neutrino flux. We perform a maximum likelihood analysis in redshift-position space to determine the significance of observed excesses of CC SNe at the location and times of IceCube neutrino alerts.

From our `SNANA` simulations of the two events, we have determined the redshift distribution of our expected signal and background populations. These distributions are displayed in Figure 5 for IC170922A and in Figure B.6 for IC171106A. The black curves in these figures will be referred to as $\xi S_z(z)$, where ξ is the IceCube signalness and $S_z(z)$ is the probability density function for signal events in redshift space given by Equation (1). The red curve, then, we express as $\xi S_z(z)\varepsilon(z)$, which folds in the optical detection efficiency as a function of redshift $\varepsilon(z)$. It is necessary at this point to introduce a signal normalization parameter λ, which will represent the total fraction of the IceCube TeV-PeV flux caused by CC SNe. Therefore, over several follow-ups, the expectation value of λ will be the fraction of IceCube neutrinos caused by CC SNe. Thus, the expected number of signal events per unit redshift is $\lambda \xi S_z(z)\varepsilon(z)$. The expected number of background events per unit redshift is the curves labelled "Remaining Background" in Figures 5 and B.6, and we express this function in our formalism as $B_z(z)$.

We distribute the events in position space according to a uniform distribution across the DECam field of view for the background population and according to a 2D asymmetric Gaussian fit to the 90% confidence interval containment region determined by IceCube for the signal population. The signal and background distributions for angular space are expressed as $S_\Omega(\Omega)$ and $B_\Omega(\Omega)$, which are normalized probability distribution functions. Therefore, $\lambda \xi S_z(z)\varepsilon(z)S_\Omega(\Omega)$ is the expected number of signal events per unit redshift per unit solid angle selected by our pipeline for a given follow-up, and $B_z(z)B_\Omega(\Omega)$ is the expected number of background events per unit redshift per unit solid angle selected by our pipeline for a given follow-up.

Suppose that after a single follow-up, we find one candidate (which we will denote as Candidate i) that passes all selection criteria. Consider two cases: redshift information being available for Candidate i and redshift information not being available for Candidate i. In these two separate cases, we can write the model-expected numbers of events as

$$m_i(\lambda) = \int dz d\Omega \; \delta(z - z_i)\delta(\Omega - \Omega_i)\left[\lambda \xi S_z(z)\varepsilon(z)S_\Omega(\Omega) + B_z(z)B_\Omega(\Omega)\right] \quad \text{with redshift information}$$
$$m_i(\lambda) = \int dz d\Omega \; \delta(\Omega - \Omega_i)\left[\lambda \xi S_z(z)\varepsilon(z)S_\Omega(\Omega) + B_z(z)B_\Omega(\Omega)\right] \qquad \text{without redshift information}$$

where we integrate from redshift $z = 0$ to $z = 1$ and over the entire DECam FoV. The delta functions serve to evaluate the expected numbers of signal and background event functions at the position and redshift of Candidate i. Therefore, in the case without available redshift information, we get contributions from all redshifts between $z = 0$ and $z = 1$. To make the discussion more straightforward, we will adopt the following shorthand notation:

$$S_i \equiv \int dz d\Omega \; \delta(z - z_i)\delta(\Omega - \Omega_i)\xi S_z(z)\varepsilon(z)S_\Omega(\Omega)$$

$$B_i \equiv \int dz d\Omega \; \delta(z - z_i)\delta(\Omega - \Omega_i)B_z(z)B_\Omega(\Omega)$$

where it is to be understood that in the case without available redshift information for Candidate i, S_i and B_i are defined without the $\delta(z - z_i)$ term, implying the need to include the contributions from all redshifts. Therefore, we can write $m_i(\lambda) = \lambda S_i + B_i$.

Now assuming the model of expected counts follows a Poisson distribution, we can write the likelihood and log-likelihood of observing k candidates in a given follow-up as the product of probabilities of observing k_j objects in

redshift-spatial bin j as

$$\mathcal{L} = \prod_{j=1}^{N \text{ bins}} \frac{[m_j(\lambda)]^{k_j} e^{-m_j(\lambda)}}{k_j!}$$

$$\implies \log(\mathcal{L}) = \sum_{j=1}^{N \text{ bins}} \log\left(\frac{[m_j(\lambda)]^{k_j} e^{-m_j(\lambda)}}{k_j!}\right)$$

$$\implies \log(\mathcal{L}) = \sum_{j=1}^{N \text{ bins}} \left(k_j \log(m_j(\lambda)) - m_j(\lambda) - \log(k_j!)\right)$$

In the limit of vanishingly small redshift-spatial bins where each bin contains either one or zero objects, we can express the log-likelihood as

$$\log(\mathcal{L}) = \left[\sum_{i=1}^{N \text{ candidates}} \log(m_i(\lambda))\right] - \int dz d\Omega \ m(\lambda)$$

where the first term comes from evaluating the $k_j \log(m_j(\lambda))$ and $\log(k_j!)$ terms for $k_j = 0$ and $k_j = 1$, and the second term is the evaluation of the sum of expected model counts overall all bins, regardless of the presence of candidates. Dropping all terms that are independent of λ, since they do not contribute in the maximization, we can write

$$\log(\mathcal{L}) = \left[\sum_{i=1}^{N \text{ candidates}} \log(\lambda S_i + B_i)\right] - f\lambda, \quad \text{where} \quad f \equiv \int dz d\Omega \ \xi S_z(z)\varepsilon(z)S_\Omega(z).$$

The value of f can be recognized as the area under the "Detected Associated" curve in Figures 5 and B.6 multiplied by the fraction of signal events that would fall on a CCD in our 2D asymmetric Gaussian distribution of signal events.

Maximizing the log likelihood with respect to λ via $\partial \log(\mathcal{L})/\partial\lambda = 0$ and multiplying by $\hat{\lambda}$, we obtain a maximization condition in terms of the individual probabilities for each candidate to be associated with the neutrino alert:

$$f\hat{\lambda} = \sum_{i=1}^{N \text{ candidates}} \frac{\hat{\lambda}S_i}{\hat{\lambda}S_i + B_i} \equiv \sum_{i=1}^{N \text{ candidates}} p_i$$

where $\hat{\lambda}$ is the optimum value of λ that satisfies this above condition. Operating under this condition that maximizes the log-likelihood, we can use the delta-log-likelihood to characterize the significance of a follow-up detecting a certain amount of excess temporally and spatially coincident CC SNe.

$$\Delta \log(\mathcal{L}) = \log(\mathcal{L})|_{\lambda=\hat{\lambda}} - \log(\mathcal{L})|_{\lambda=0}$$

Over a sequence of follow-up observations, then, we define our test statistic (TS) to be the sum of the delta-log-likelihoods of all the constituent follow-ups.

$$\text{TS} = \sum_{n=1}^{N \text{ follow-ups}} (\Delta \log(\mathcal{L}))_n.$$

For a follow-up campaign that observes a given number of SNe candidates, then, we can evaluate the significance of the claim that the number of candidates observed is greater than the expected background and hence likely linked to the IceCube neutrino alerts by comparing the calculated TS value to the null-hypothesis TS distribution. In this work, we obtain the null-hypothesis TS distribution by performing 1000 realizations of follow-up campaigns with λ set to 0.0. To obtain our signal-hypothesis TS value for a given value of λ we perform the 1000 realizations and take the median of the distribution to be our signal TS value. The p-value for this test is the fraction of the null-hypothesis distribution that is larger than the median signal-hypothesis TS value, allowing for a direct evaluation of the significance level at which we can claim CC SNe contribute to the TeV-PeV IceCube neutrino flux.

20

B. ADDITIONAL FIGURES
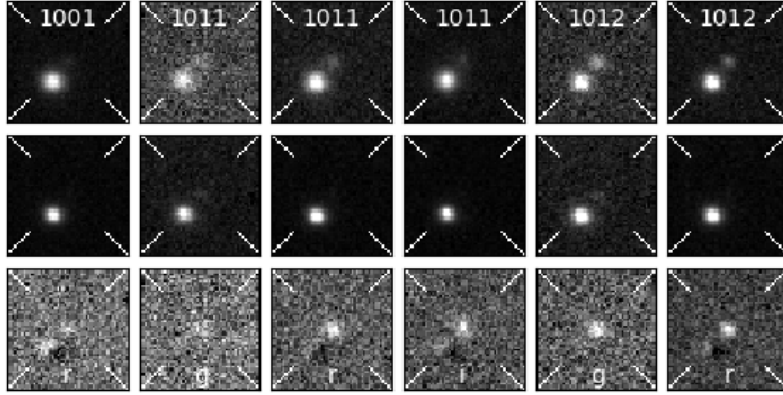
Figure B.1. Image stamps for DES-Cand-1. The top row is the search image, the middle row is the template, and the bottom row is the difference image. Filters are shown at the bottom of each column and dates are given in MMDD format at the top of each column.
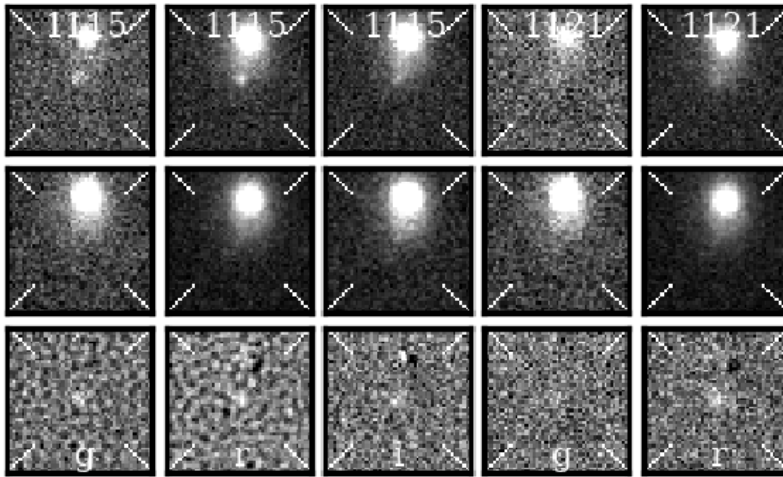

Figure B.2. Image stamps for DES-Cand-2. The top row is the search image, the middle row is the template, and the bottom row is the difference image. Filters are shown at the bottom of each column and dates are given in MMDD format at the top of each column.
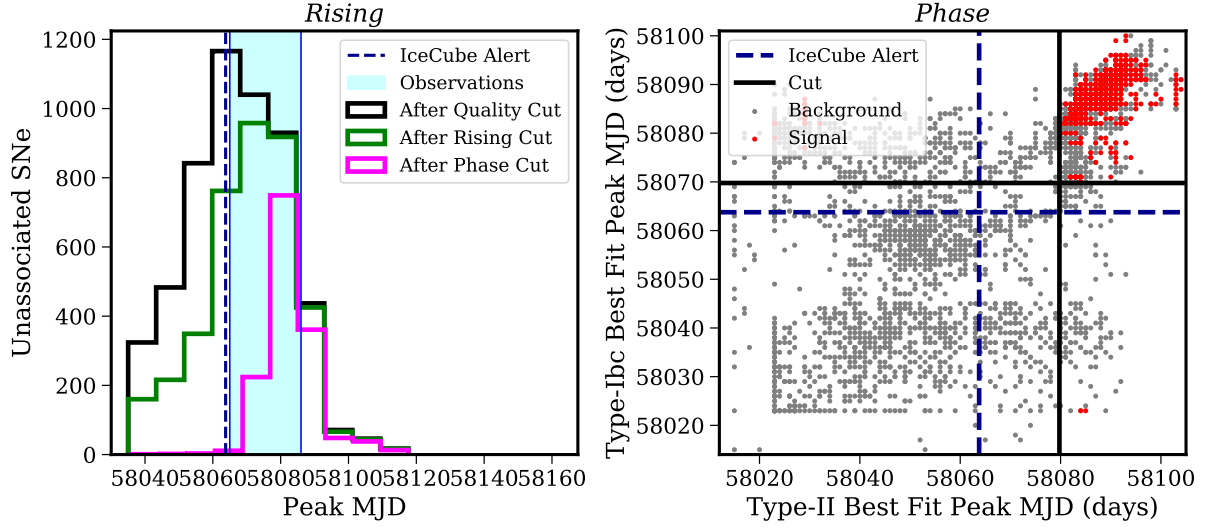
Figure B.3. The efficacies of the rising and phase cuts applied to the IC171106A simulations. The number of reported events is amplified by a factor of 500 as compared to a typical DECam field of view.
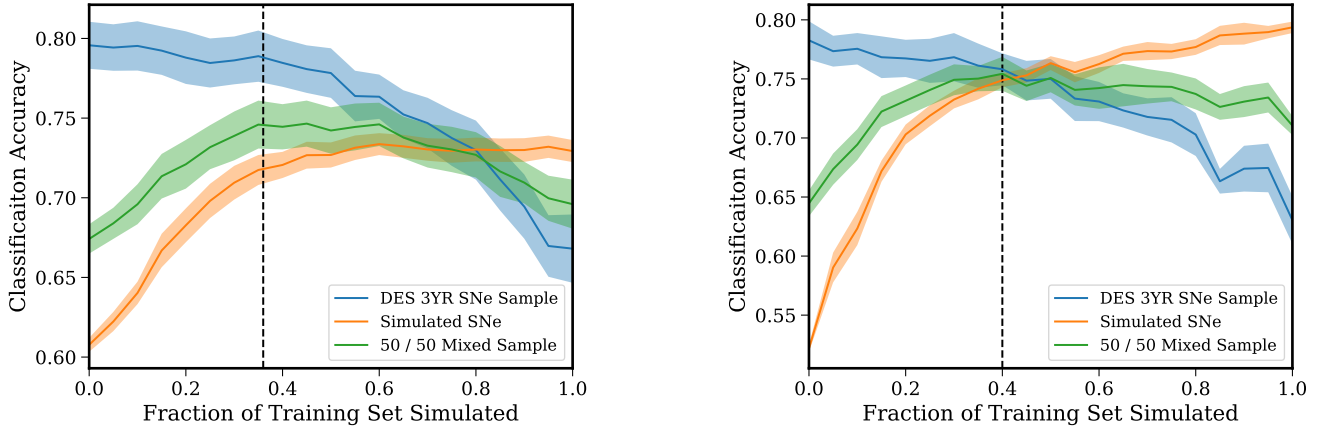

Figure B.4. Classifier accuracy for real SNe, simulated SNe, and a mixed sample parameterized by the fraction of the training set composed of simulated SNe. The optimum fraction chosen for training is shown by the black dashed line. *Left:* Based on the IC170922A follow-up. *Right:* Based on the IC171106A follow-up.
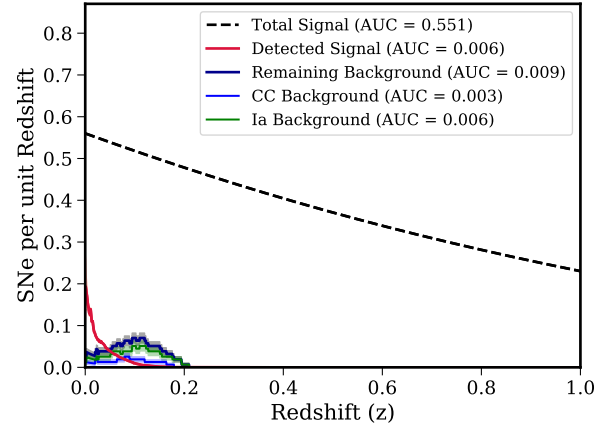
22
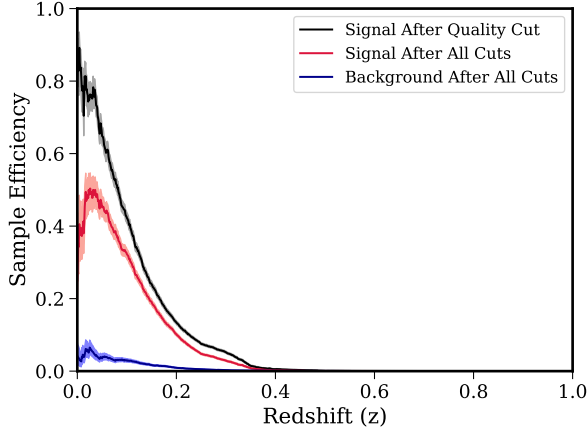
Figure B.5. Detection efficiency parameterized by redshift for the signal and background populations for the IC171106A alert follow-up.
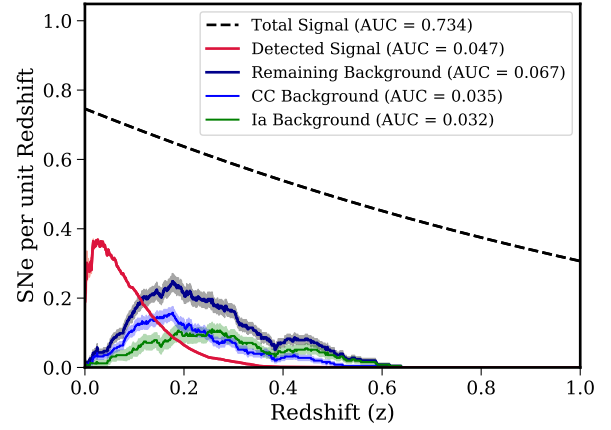

Figure B.6. Expected events at a given redshift based on simulations of the IC171106A follow-up.
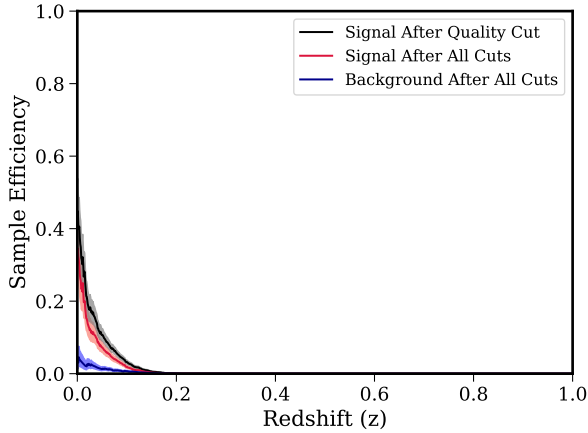
Figure B.7. The detection efficiency as a function of redshift for simulations of IC170922A with a limiting magnitude of 21 mag.

Figure B.8. Expected events at a given redshift based on simulations of the IC170922A follow-up with limiting magnitue 21. Shaded error regions give a 68% confidence interval for the signal curve and a standard Poisson statistical uncertainty for the background curves.
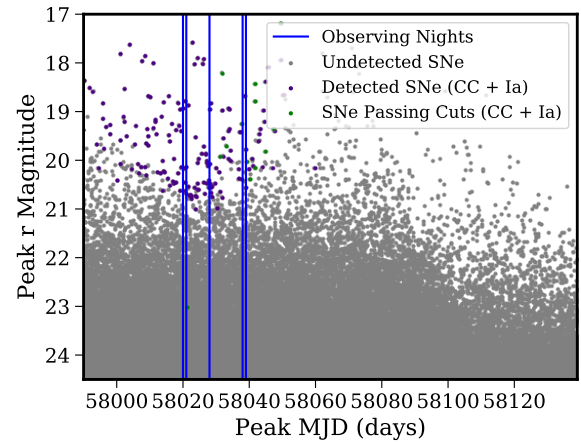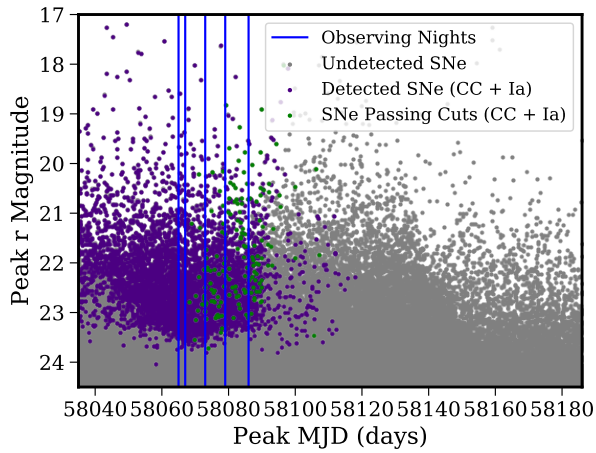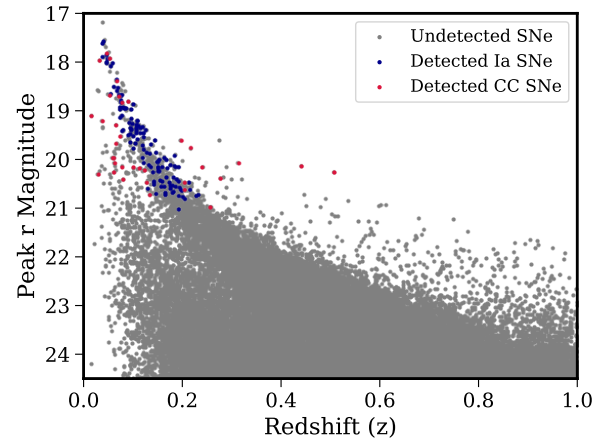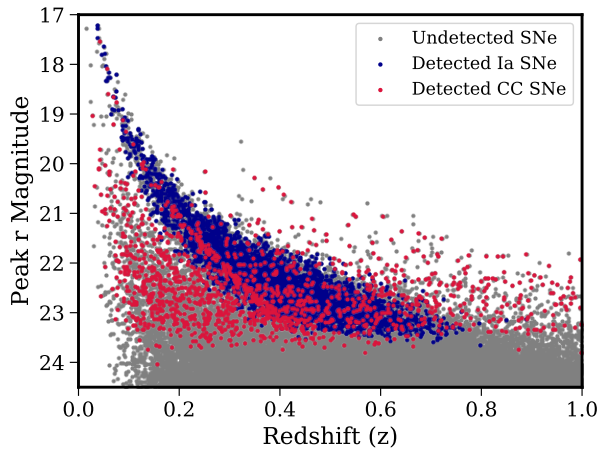
Figure B.9. The background SNe distribution for simulations of IC171106A with a limiting magnitude of 23.5 mag

Figure B.10. The background SNe distribution for simulations of IC170922A with a limiting magnitude of 21 mag.

REFERENCES

Aartsen, M., Ackermann, M., Adams, J., et al. 2017a, Astroparticle Physics, 92, 30

Aartsen, M. G., Abbasi, R., Ackermann, M., et al. 2014, Journal of Instrumentation, 9, P03009

Aartsen, M. G., Abraham, K., Ackermann, M., et al. 2015a, The Astrophysical Journal, 809, 98

Aartsen, M. G., Ackermann, M., Adams, J., et al. 2015b, The Astrophysical Journal Letters, 805, L5

Aartsen, M. G., Abraham, K., Ackermann, M., et al. 2015c, The Astrophysical Journal, 811, 52

—. 2017b, The Astrophysical Journal, 835, 45

—. 2017c, The Astrophysical Journal, 835, 151

Abbasi, R., Abdou, Y., Abu-Zayyad, T., et al. 2011, Phys. Rev. D, 84, 082001

Abbasi, R., Abdou, Y., Abu-Zayyad, T., et al. 2012, A&A, 539, A60

Adrián-Martínez, S., Ageron, M., Albert, A., et al. 2016, Journal of Cosmology and Astroparticle Physics, 2016, 062

Ahlers, M., Bai, Y., Barger, V., & Lu, R. 2016, Phys. Rev. D, 93, 013009

Ando, S., & Beacom, J. F. 2005, Phys. Rev. Lett., 95, 061103

Bailey, S., Aragon, C., Romano, R., et al. 2007, The Astrophysical Journal, 665, 1246

Baret, B., & Elewyck, V. V. 2011, Reports on Progress in Physics, 74, 046902

Barthelmy, S. D., Butterworth, P., Cline, T. L., et al. 1998, AIP Conference Proceedings, 428, 99

Beall, J. H. 2006, Chinese Journal of Astronomy and Astrophysics, 6, 174

Bechtol, K., Ahlers, M., Mauro, M. D., Ajello, M., & Vandenbroucke, J. 2017, The Astrophysical Journal, 836, 47

Bernstein, J. P., Kessler, R., Kuhlmann, S., et al. 2012, The Astrophysical Journal, 753, 152

Breiman, L. 2001, Machine Learning, 45, 5

Burrows, A., Hayes, J., & Fryxell, B. A. 1995, ApJ, 450, 830

Caprioli, D. 2015, The Astrophysical Journal Letters, 811, L38

Chiarusi, T., & Spurio, M. 2010, The European Physical Journal C, 65, 649

Dermer, C. D., & Atoyan, A. 2003, Phys. Rev. Lett., 91, 071102

DES Collaboration. 2018a, 872, L30

—. 2018b, Phys. Rev. D, 98, 043526

DES Collaboration et al. 2019, arXiv e-prints

Dilday, B., Kessler, R., Frieman, J. A., et al. 2008, The Astrophysical Journal, 682, 262

Flaugher, B., Diehl, H. T., Honscheid, K., et al. 2015, AJ, 150, 150

Franckowiak, A. 2017, Journal of Physics: Conference Series, 888, 012009

Gaisser, T. K., & Stanev, T. 1987, Phys. Rev. Lett., 58, 1695

Goldstein, D. A., D'Andrea, C. B., Fischer, J. A., et al. 2015, AJ, 150, 82

González-Gaitán, S., Tominaga, N., Molina, J., et al. 2015, Monthly Notices of the Royal Astronomical Society, 451, 2212

Guy, Sullivan, M., Conley, A., et al. 2010, A&A, 523, A7

Halzen, F. 2016, Nature Physics, 13, 232 EP

Hunter, J. D. 2007, Computing In Science & Engineering, 9, 90

IceCube, Aartsen, M. G., Ackermann, M., et al. 2017, A&A, 607, A115

IceCube Collaboration. 2013, Science, 342

—. 2018a, doi:10.21234/B4KS6S, dataset

—. 2018b, Science, 361

IceCube Collaboration, Fermi-LAT, MAGIC, et al. 2018, Science, 361

Jones, E., Oliphant, T., Peterson, P., et al. 2001, SciPy: Open source scientific tools for Python, ,

Kankare, E., Huber, M., Smartt, S. J., et al. 2019, A&A (Submitted Jan 2019)

Keivani, A., Ayala, H., & DeLaunay, J. 2017, ArXiv e-prints, arXiv:1708.04724

Kessler, R., Bernstein, J. P., Cinabro, D., et al. 2009, Publications of the Astronomical Society of the Pacific, 121, 1028

Kessler, R., Bassett, B., Belov, P., et al. 2010, Publications of the Astronomical Society of the Pacific, 122, 1415

Kessler, R., Marriner, J., Childress, M., et al. 2015, The Astronomical Journal, 150, 172

Kowalski, M., & Mohr, A. 2007, Astropart. Phys., 27, 533

Li, W., Leaman, J., Chornock, R., et al. 2011, Monthly Notices of the Royal Astronomical Society, 412, 1441

Madau, P., & Dickinson, M. 2014, Annual Review of Astronomy and Astrophysics, 52, 415

McKinney, W. 2010, in Proceedings of the 9th Python in Science Conference, ed. S. van der Walt & J. Millman, 51 – 56

Mészáros, P., & Waxman, E. 2001, Phys. Rev. Lett., 87, 171102

Mohr et al., Robert Armstrong, E. B. G. D. S. D. M. G. R. G. W. H. N. K. H. L. J. M. D. P. I. S. M. S. T. T. D. T. B. Y. 2012, 8451

Murase, K., & Ioka, K. 2013, Phys. Rev. Lett., 111, 121102

Murase, K., Oikonomou, F., & Petropoulou, M. 2018, ArXiv e-prints, arXiv:1807.04748, accepted to ApJ

Pedregosa, F., Varoquaux, G., Gramfort, A., et al. 2011, Journal of Machine Learning Research, 12, 2825

Razzaque, S., Mészáros, P., & Waxman, E. 2004, Phys. Rev. Lett., 93, 181101

Sadeh, I., Abdalla, F. B., & Lahav, O. 2016, Publications of the Astronomical Society of the Pacific, 128, 104502

Sako, M., Bassett, B., Connolly, B., et al. 2011, The Astrophysical Journal, 738, 162

Senno, N., Murase, K., & Mészáros, P. 2016, Phys. Rev. D, 93, 083003

Silberberg, R., & Shapiro, M. M. 1979, International Cosmic Ray Conference, 10, 357

Smith, M., Fox, D., Cowen, D., et al. 2013, Astroparticle Physics, 45, 56

Strigari, L. E., Beacom, J. F., Walker, T. P., & Zhang, P. 2005, Journal of Cosmology and Astroparticle Physics, 2005, 017

Strotjohann, N. L., Kowalski, M., & Franckowiak, A. 2019, Astron. Astrophys., 622, L9

Tamborra, I., & Ando, S. 2016, Phys. Rev. D, 93, 053010

Thompson, T. A., Burrows, A., & Pinto, P. A. 2003, The Astrophysical Journal, 592, 434

Tipping, M. E., & Bishop, C. M. 1999, Journal of the Royal Statistical Society: Series B (Statistical Methodology), 61, 611

Van Der Walt, S., Colbert, S. C., & Varoquaux, G. 2011, Computing in Science & Engineering, 13, 22

Woosley, S., & Janka, T. 2005, Nature Physics, 1, 147 EP